

# U–Pb zircon geochronology and phase equilibria modelling of a mafic eclogite from the Sumdo complex of south-east Tibet: insights into prograde zircon growth and the assembly of the Tibetan plateau

O.M. Weller<sup>a,b,\*</sup>, M.R. St-Onge<sup>a</sup>, N. Rayner<sup>a</sup>, D.J. Waters<sup>b</sup>, M.P. Searle<sup>b</sup>, R.M. Palin<sup>c</sup>

<sup>a</sup>*Geological Survey of Canada, 601 Booth Street, Ottawa, Ontario, K1A 0E8, Canada*

<sup>b</sup>*Department of Earth Sciences, University of Oxford, South Parks Road, Oxford, OX1 3AN, United Kingdom*

<sup>c</sup>*Institute of Geosciences, Johannes-Gutenberg University Mainz, Mainz, 55128, Germany*

---

## Abstract

The Sumdo complex is a Permian–Triassic eclogitic metamorphic belt in south-east Tibet, which marks the location of a suture zone that separates the northern and southern Lhasa terranes. An integrated geochronological and petrological study of a mafic eclogite from the complex has constrained its tectonometamorphic history and provides a case study of zircon growth in eclogite as a product of prograde dissolution–precipitation. *In situ* U–Pb geochronology indicates that the eclogite contains a single population of zircon with a crystallisation age of  $273.6 \pm 2.8$  Ma. The morphology and chemistry of the zircon grains are consistent with growth by dissolution–precipitation of protolith magmatic zircon. The presence of zircon grains as inclusions in the cores of peak phases indicates that zircon dissolution–precipitation occurred during prograde metamorphism, and calculated pressure and temperature conditions over which mineral inclusions in zircon are stable suggest that the zircon most likely precipitated at  $\sim 15.5$ – $16.5$  kbar and  $500$ – $560$  °C. Subsequent peak metamorphism is calculated to have reached pressure–temperature conditions of  $27 \pm 1$  kbar and  $670 \pm 50$  °C. Previous studies, which have documented a range of peak metamorphic conditions from high- to ultra-high pressure at *c.* 266–230 Ma, indicate that the Sumdo complex is a composite belt that experienced protracted eclogite exhumation. The results of this study are consistent with this interpretation, and extend the age range of high-pressure metamorphism in the complex to over 40 Myr. Analysis of published pressure–temperature–time data indicates two systematic behaviours within this spread. First, peak

---

\*Corresponding author. Tel: +1 613 601 0191  
Email address: owen.weller@canada.ca (O.M. Weller)

metamorphic temperatures declined over time. Second, eclogite exhumation occurred in two discrete intervals: soon after formation, and during the demise of the subduction zone. The latter behaviour serves as a reminder that eclogite exhumation is the exception rather than the rule.

*Keywords:* Tibetan Plateau, Sumdo complex, U–Pb zircon, eclogite-facies metamorphism, zircon dissolution–precipitation

---

## 1. Introduction

The Sumdo complex is an east-trending, high- to ultra-high pressure (UHP) eclogite-bearing metamorphic belt that extends for over 40 km in the middle of the Lhasa composite terrane in southern Tibet (Fig. 1; Yang et al., 2009; Cheng et al., 2012). The complex is thought to have been metamorphosed in a subduction zone during the Permian–Triassic, leading to a reinterpretation of the Lhasa domain—previously considered a single tectonic element rifted from Gondwana—as a composite tectonic unit, composed of northern and southern parts (Yang et al., 2009; Zeng et al., 2009). The tectonostratigraphic assemblages associated with the medial Lhasa suture, its structural elements and its thermal and geochronological evolution nevertheless remain poorly resolved. Understanding the tectonometamorphic history of the Lhasa composite terrane is important as it occupies a key position in the Himalayan–Tibetan orogen, being on the leading edge of the amalgamated Asian plate prior to Cenozoic collision with India (Yin and Harrison, 2000).

In this contribution we integrate U–Pb zircon geochronology and phase equilibria modelling to explore the timing and pressure–temperature ( $P$ – $T$ ) conditions of eclogite-facies metamorphism in the Sumdo complex. The results presented herein characterise the prograde, peak and retrograde metamorphic conditions of a mafic eclogite sample from the complex, illustrate the importance of petrochronology for interpreting a metamorphic zircon age and develop our understanding of the assembly of the Tibetan plateau.

## 20 **2. Geological Setting**

21 The Sumdo complex is an east-trending, Permian–Triassic eclogitic metamorphic belt in south-  
22 east Tibet, which marks the location of the Luobadui–Milashan suture zone that separates the  
23 northern and southern Lhasa terranes (yellow star, Fig. 1a). The complex dominantly com-  
24 prises quartzite and semi-pelitic schist, with minor marble, metabasic lenses and serpentinised  
25 ultramafic blocks (Fig. 1b, Yang et al., 2009). The metabasic lenses form 1–30 m long boudins  
26 hosted by metasedimentary strata, with eclogite-facies mineral assemblages preserved in boudin  
27 cores that transition to lower-pressure garnet-amphibolite at the rims (Fig. 2a). The basaltic  
28 protolith of the eclogite boudins has been interpreted based on its major- and trace-element geo-  
29 chemistry to have a mid-ocean ridge (MOR; Yang et al., 2009) or ocean island affinity (Cheng  
30 et al., 2015), and likely formed at *c.* 304–291 Ma (U–Pb zircon cores; Cheng et al., 2012, 2015)  
31 in a MOR or back-arc basin setting (Yang et al., 2009; Cheng et al., 2015). Laterally extensive  
32 Carboniferous continental rift-related volcanic rocks and Permian arc-related andesites crop out  
33 discontinuously in a subparallel east-trending belt  $\sim$ 30–50 km north of the Sumdo complex  
34 (Yang et al., 2009). Based on these spatial associations, Yang et al. (2009) interpreted eclogite-  
35 facies metamorphism to have occurred in a north-dipping subduction zone that was established  
36 beneath the north Lhasa terrane during the early Permian.

37 Several eclogite localities have been studied in the Sumdo complex. The highest-pressure condi-  
38 tions are reported from rocks exposed at Jilang (Fig. 1b), with peak metamorphic UHP condi-  
39 tions of 3.4–3.8 GPa and 750–790 °C at  $265.9 \pm 1.1$  Ma (Lu–Hf whole-rock–garnet–omphacite)  
40 suggested for a coesite-bearing sample (Cheng et al., 2012), suggesting subduction to a depth  
41 of 120 km. For the Sumdo eclogite locality, near-UHP peak metamorphic conditions of  $\sim$ 2.7  
42 GPa and 730 °C at  $262 \pm 5$  Ma (U–Pb zircon) have been reported (Yang et al., 2009). Cooler  
43 peak conditions of  $\sim$ 2.6 GPa and 465–505 °C at  $230.0 \pm 4.7$  Ma (Sm–Nd whole-rock–garnet–  
44 omphacite) have been proposed for a glaucophane-bearing eclogite sample from the Bailang  
45 region (Fig. 1b; Cheng et al., 2015). Finally, peak conditions of  $\sim$ 2.6 GPa and 650 °C at  $239$   
46  $\pm 3.5$  Ma (Sm–Nd whole-rock–garnet–omphacite) have been suggested for an eclogite sample  
47 from the complex (location not specified; Zeng et al., 2009). Cheng et al. (2015) interpreted  
48 the scatter in peak *P–T*-time estimates to reflect that the Sumdo complex comprises multiple

49 tectonic slices.

50 Accretion of the north and south Lhasa terranes and exhumation of the Sumdo complex along  
51 the Luobadui-Milashan suture (Fig. 1a) is proposed to have occurred at *c.* 241–224 Ma, based  
52 on similar muscovite Ar–Ar cooling ages from all units in the complex (Li et al., 2012). This was  
53 followed by widespread late Triassic–early Jurassic regional amphibolite-facies metamorphism  
54 and granite plutonism, primarily to the north of the Sumdo complex (Dong et al., 2011; Li et al.,  
55 2012; Lin et al., 2013; Weller et al., 2015a, 2016).

### 56 **3. Petrography and mineral chemistry**

#### 57 *3.1. Analytical techniques*

58 Sample nt2 was collected from the Sumdo eclogite locality (Fig. 1b; 29.873 °N, 92.526 °E).  
59 Representative images of typical microstructural features and assemblages are given in Fig. 2.  
60 Modal abundances of major rock-forming minerals were calculated by point counting multiple  
61 thin sections with randomised 500-point grids using the software JMicroVision (Roduit, 2010).  
62 Whole-rock major element data (Table 1) were acquired using X-ray fluorescence (XRF) con-  
63 ducted on a fused glass bead made from a powdered 1 kg portion of the sample with a Rigaku®  
64 RIX-2000 spectrometer at the Department of Geosciences, National Taiwan University, follow-  
65 ing the analytical procedure of Wang et al. (2004). Major element mineral compositional data  
66 (Table 2) were acquired using a JEOL JSM-840A scanning electron microscope (SEM) fitted  
67 with an Oxford Instruments Isis 300 energy-dispersive analytical system (EDS) at the Depart-  
68 ment of Earth Sciences, University of Oxford. Accelerating voltage was 20 kV, with a beam  
69 current of 6 nA and a live counting time of 100 seconds. The SEM was calibrated with a  
70 range of natural and synthetic standards, and a ZAF correction procedure was used. The beam  
71 current was checked regularly and the count rate calibrated every 120 minutes using a cobalt  
72 metal standard. All mineral cation totals were calculated using AX (Holland, 2009) and min-  
73 eral abbreviations follow Whitney and Evans (2010). Anhydrous mineral compositions were  
74 calculated to standard numbers of oxygen per formula unit (pfu), whereas white mica analyses  
75 were calculated to a total of 11, amphibole to 23 and epidote to 25. Compositional profiles



across garnet (Fig. 3) were determined by accumulating counts along a 256-channel line scan for approximately 30 minutes. The profiles were background-corrected and calibrated against six point analyses taken along the profile. Major and trace element mineral composition data were acquired for ilmenite, rutile and titanite (Table S1) using a JEOL JXA-8230 electron microprobe equipped with five wavelength-dispersive spectrometers (WDS) at the Department of Geological Sciences and Geological Engineering, Queen's University. Accelerating voltage was 15 kV, with a beam current of 30 nA and a live counting time of 250 seconds. Standards were a mix of natural and synthetic minerals and metals, and a PAP correction procedure was applied.

### 3.2. *nt2*

Sample nt2 is a massive, medium- to coarse-grained mafic eclogite composed of garnet (38 vol.%), calcic-amphibole (28 vol.%), omphacite (12 vol.%), phengite (12 vol.%), rutile (3 vol.%), epidote (2 vol.%), quartz (2 vol.%), titanite (2 vol.%) and apatite (1 vol.%), with minor biotite, chlorite, ilmenite, talc and zircon (Fig. 2b).

Garnet occurs as subhedral to anhedral porphyroblasts that are approximately 0.5–3 mm in diameter. Core domains are inclusion-rich, and contain apatite, biotite, chlorite, phengite, quartz, rutile, talc, titanite and zircon, whereas rim domains are inclusion-poor, and contain minor phengite, quartz, rutile, talc and zircon (Fig. 2c,d). Grains are commonly heavily fractured, particularly in core regions (e.g. Fig. 2c), with calcic amphibole, chlorite, epidote and phengite present as retrogressive infill.

Garnet chemical zoning is moderately variable between grains, but where Mn is observed to be decreasing from core–rim, consistent core–rim patterns are observed. For example, in Fig. 3c, the stippled core region is characterised by a rimwards increase in Mn, alongside decreasing Mg, increasing Ca and decreasing Fe content, which are trends that are not reproducible between all grains. These patterns could be due to modification of garnet core chemistry by fluid-assisted mass transfer along now-healed fractures during retrograde metamorphism, which has been suggested to be a situation transitional to the formation of atoll garnets (Waters and Utting, 2016). However, from the point at which Mn starts to decrease rimwards (label A, Fig. 3c), the chemical trends are typical of all analysed grains, with Mg increasing, Ca decreasing and

104 Fe first increasing then decreasing towards the rim. Consequently, the values of Ca ( $\sim 35\%$ )  
 105 and Mg ( $\sim 8\%$ ) at the position of highest Mn content ( $\sim 3\%$ ) are considered the most reliable  
 106 primitive garnet compositions. The inclusion-poor rims of garnet grains are notable for having  
 107 sharply increasing Mg up to  $\sim 23\%$ , compared with relatively flat Ca contents between  $\sim 25$  to  
 108  $28\%$ . The absence of compositional inflections in Mn at the outermost rim indicates that the  
 109 preserved compositions should represent those obtained at peak metamorphic conditions (cf.  
 110 Kohn and Spear, 2000).

111 Omphacite forms anhedral porphyroblasts, with a jadeite content ( $\text{Na}/(\text{Na} + \text{Ca})$ ) that in-  
 112 creases from 0.25 in the cores of large grains to 0.29 towards the rim (Table 2). Amphibole is  
 113 present as spongy quartz–amphibole (hornblende–edenite–pargasite) intergrowths that embay  
 114 into omphacite grains, which progressively grade into zoned amphibole plates, comprised of light  
 115 green actinolite cores and dark green pargasite rims that embay into garnet grains (Fig. 2b,e;  
 116 Table 2). These textural relations are interpreted as the replacement of peak eclogite-facies  
 117 minerals by amphibole during retrograde metamorphism (Palin et al., 2014). Matrix phengite  
 118 exhibits a core to rim decrease in Si from 3.50 to 3.42 pfu (per 11 oxygens). As phengite content  
 119 typically increases with pressure, this reverse zonation suggests some phengite growth and/or  
 120 re-equilibration during decompression, with the highest phengite content considered the most  
 121 representative of peak conditions. Titanium-bearing phases vary with petrographic position,  
 122 with titanite included in garnet cores, rutile included in garnet cores and rims (Fig. 2f), and  
 123 matrix rutile replaced at its rims by granular ilmenite and films of titanite (Fig. 2g). Titanite  
 124 inclusions in garnet cores are interpreted as prograde, rutile as a peak phase, and ilmenite and  
 125 matrix titanite as sequential retrograde phases. Notably, titanite and rutile inclusions in garnet  
 126 contain higher Zr contents than their matrix counterparts (Table S1). Quartz occurs in both the  
 127 matrix and as inclusions in garnet, but no coesite (or evidence for former coesite) was observed.  
 128 Finally, epidote porphyroblasts are observed in the matrix in amphibole-rich regions and are  
 129 interpreted as retrogressive (Palin et al., 2014).

## 4. U–Pb zircon geochronology

### 4.1. Analytical techniques

*In situ* U–Pb isotopic analyses of zircon in sample nt2 were carried out using a sensitive high-resolution ion microprobe (SHRIMP), which preserves the petrographic context of obtained age data, at the Geological Survey of Canada (GSC). Automated full thin section scans were performed on the GSC’s Zeiss Evo SEM in order to locate zircon suitable for geochronological analysis. Targets from all petrographic contexts were then prepared for analysis according to the methods of Rayner and Stern (2002). Backscattered electron and cathodoluminescence (CL) images were generated for each zircon grain to identify internal compositional domains, and to guide analytical spot placement (Fig. 4). SHRIMP zircon analysis employed the instrumental conditions described in Stern (1997). Analytical details regarding spot size, data reduction protocol and U–Pb calibration are reported in Table 3. Isotopic data were interpreted using a Tera-Wasserburg diagram (Fig. 5), which was generated using Isoplot (version 3.0; Ludwig, 2003).

### 4.2. Results

Zircon in sample nt2 forms subhedral grains 100–300  $\mu\text{m}$  in diameter that are present as inclusions in garnet and omphacite, and throughout the matrix (Fig. 4a–d; Table 3). The grains are commonly inclusion-rich, containing micron-scale biotite, chlorite, muscovite, quartz and rutile grains (Fig. 4e–h), and exhibit irregular and diffuse ‘mosaic-type’ CL patterns (Fig. 4i–l; Corfu, 2003; Rubatto et al., 2008). Twenty-eight analyses were made of 23 zircon grains in a variety of petrographic positions in the sample (Table 3). A free regression through the common-Pb uncorrected dataset using a Tera-Wasserburg diagram yielded a lower intercept age of  $273.6 \pm 2.8$  Ma ( $n = 25$ , MSWD = 1.5, 95 % confidence; Fig. 5). Three grains gave non-reproducible younger ages (1-9, 3-11, 7-1; Table 3), which are attributed to  $^{206}\text{Pb}$  loss, and these analyses were excluded from the regression (dashed ellipses, Fig. 5).

The simple observation that the analysed zircon grains contain inclusions of metamorphic minerals and are themselves included in the cores of garnet and omphacite indicate that the zircon

grew during prograde metamorphism, thus the  $273.6 \pm 2.8$  Ma age provides a minimum age constraint for the timing of eclogite-facies metamorphism of the sample. Notably, the inclusion-rich, spongy nature of the zircons and their diffuse ‘mosaic-type’ CL patterns are typical of zircon that has grown by recrystallisation of protolith magmatic zircon by subsolidus dissolution–precipitation under the influence of metamorphic fluids (Rubatto et al., 2008). We suggest that this growth mechanism is consistent with the variable chemistry of the grains, which exhibit both igneous ( $> 0.1$ ) and metamorphic ( $< 0.1$ ) Th/U ratios that range from 0.01 to 1.62 (Table 3; Corfu, 2003), despite defining a single age. Furthermore, the analysed zircon grains contain highly variable contents of Hf (8484–18722 ppm, Table 3) and Yb (38–1279 ppm, Table 3), which range from arguably more metamorphic-style (low values) to igneous-style (high values) in character. We attribute all of these features to recrystallisation of magmatic zircon by dissolution–precipitation, which yielded mixed igneous–metamorphic chemical signatures, but nevertheless defines a single age: the timing of recrystallisation. Further discussion of the zircon age with respect to the  $P$ – $T$  history and thence the Zr budget of the sample is given below.

## 5. Phase equilibria modelling

### 5.1. Analytical techniques

To constrain the stability of mineral inclusion suites entrapped in zircon and to provide an estimate of peak metamorphic conditions, a  $P$ – $T$  equilibrium phase diagram was constructed for sample nt2 using THERMOCALC v3.40 and the internally-consistent dataset tc-ds55 (Holland and Powell, 1998; updated to August, 2004). Modelling was performed in the  $\text{Na}_2\text{O}$ – $\text{CaO}$ – $\text{K}_2\text{O}$ – $\text{FeO}$ – $\text{MgO}$ – $\text{Al}_2\text{O}_3$ – $\text{SiO}_2$ – $\text{H}_2\text{O}$ – $\text{TiO}_2$ – $\text{O}$  (NCKFMASHTO) system using the following activity–composition models: biotite and garnet (White et al., 2007); chlorite (Holland et al., 1998); actinolite–glaucophane–hornblende and diopside–omphacite–jadeite (Diener and Powell, 2012); epidote and talc (Holland and Powell, 1998); ilmenite–hematite (White et al., 2000); plagioclase–K-feldspar (Holland and Powell, 2003); and muscovite–paragonite (Coggon and Holland, 2002). Albite, coesite,  $\text{H}_2\text{O}$ , lawsonite, quartz, rutile, titanite and zoisite were considered as pure phases.

185 The effective bulk composition used for sample nt2 was calculated by modification of the whole-  
 186 rock XRF analysis (Table 1), taking into consideration the contribution of unmodelled accessory  
 187 phases and oxides, and ferric iron content (cf. Weller et al., 2013). First,  $P_2O_5$  was removed  
 188 from the bulk and total CaO proportionally adjusted to correct for the contribution made by  
 189 apatite, with all measured  $P_2O_5$  considered to have been derived from apatite. Second, a value  
 190 of  $X_{Fe^{3+}}$  (molar  $Fe^{3+}/Fe_{total}$ ) of 0.10 was applied, using the Fe-oxide minerals present as a  
 191 guide to oxidation state (White et al., 2000; Diener and Powell, 2010), with the value adjusted  
 192 to satisfactorily reproduce the observed mineral assemblages and mineral compositions (e.g.  
 193 Endo et al., 2012). This yielded an input composition (mol. %) of:  $SiO_2$  - 47.08,  $Al_2O_3$  - 9.75,  
 194  $CaO$  - 12.89,  $MgO$  - 11.35,  $FeO^{total}$  - 13.99,  $K_2O$  - 0.52,  $Na_2O$  - 1.36,  $TiO_2$  - 2.35 and  $O$  -  
 195 0.70, with  $H_2O$  considered to be in excess due to the widespread presence of hydrous prograde,  
 196 peak and retrograde phases. Consideration of restricted  $H_2O$  contents and the effect of cation  
 197 sequestration into growing garnet porphyroblasts are discussed below, and a  $T$ - $M_{H_2O}$  phase  
 198 diagram is shown and described in Fig. S1.  $MnO$  was not included as a component due to its  
 199 low concentration in the sample (Table 1). Although it is acknowledged that consideration of  
 200  $MnO$  would affect the stability field of garnet, the lack of Mn-bearing activity models for other  
 201 major eclogite-facies minerals (amphibole, clinopyroxene and white mica) precludes examination  
 202 of partitioning between these phases (St-Onge et al., 2013). A temperature of 725 °C was used  
 203 as an upper limit in the calculations, given the current lack of activity–composition models  
 204 suitable for describing suprasolidus phase relations in metabasic lithologies.

## 205 5.2. Results

206 A  $P$ - $T$  phase equilibria diagram was constructed for sample nt2 (Fig. 6) between 5–30 kbar  
 207 and 475–725 °C, to provide a general framework with which to interpret prograde, peak and  
 208 retrograde features of the sample, including inclusion suites, with the observed peak assemblage  
 209 Cpx–Grt–Ms–Qz–Rt highlighted in red. Due consideration as to how the effective bulk compo-  
 210 sition, thus the topology of Fig. 6, may have departed from the modified-XRF bulk composition  
 211 is given below.

### 212 5.2.1. Zircon recrystallisation

213 To evaluate the probable  $P$ – $T$  conditions of zircon recrystallisation in sample nt2, equilibrium  
214 assemblages on Fig. 6 were identified that contain all of the minerals that occur as inclusions in  
215 zircon grains (biotite, chlorite, quartz, muscovite and rutile; Fig. 4e–h). This approach makes  
216 the simplifying assumption that the observed inclusion suite represents a compatible equilibrium  
217 assemblage, based on the single age obtained for the zircon population. Only one region of  $P$ –  
218  $T$  space contains the observed inclusion suite, highlighted in orange on Fig. 7. This suggests  
219 that zircon dissolution–precipitation most likely occurred at  $\sim 15.5$ – $16.5$  kbar and  $500$ – $560$  °C.  
220 The interpretation of zircon in sample nt2 having recrystallised in a single event represents a  
221 simple end member as the  $\pm 2.8$  Myr age error on the zircon determination (Fig. 5) means that  
222 protracted or episodic zircon growth within a 5.6 Myr interval is not resolvable with the precision  
223 of the present technique. Nevertheless, the suggested  $P$ – $T$  conditions of recrystallisation are  
224 consistent with the general inference that the zircon age dates prograde metamorphism as the  
225 inclusion suite stability field is located at lower temperatures and pressures relative to the peak  
226 field (red text, Fig. 6). Sub-solidus zircon dissolution–precipitation implies the catalytic presence  
227 of a fluid, either derived internally from prograde dehydration reactions or sourced externally  
228 (Rubatto et al., 2008). This in turn implies that the assumption of excess  $H_2O$  is justifiable at  
229 the  $P$ – $T$  conditions of recrystallisation.

### 230 5.2.2. Prograde–peak–retrograde $P$ – $T$ conditions

231 To constrain prograde  $P$ – $T$  conditions for sample nt2, garnet compositional isopleths are shown  
232 on Fig. 8, and compared with the preserved compositional zonation in garnet rim domains shown  
233 in Fig. 3c, with labels A and B on Fig. 8 corresponding to the equivalent labels (renormalised  
234 without Mn) on Fig. 3c. We acknowledge that this prograde path is qualitative as the model  
235 does not account for garnet cation sequestration, and given that the  $P$ – $T$  path enters the field  
236 of lawsonite stability (which was not observed in sample nt2),  $H_2O$ -undersaturated conditions  
237 would likely have been encountered at some point during this interval (e.g. Clarke et al.,  
238 2006; Weller et al., 2015b). However, the proposed  $P$ – $T$  path does serve to illustrate that  
239 the preserved zonation provides a plausible link between suggested  $P$ – $T$  conditions of zircon

240 recrystallisation (orange shading, Fig. 8) and the peak assemblage field of the sample, both  
 241 of which are suggested to have been characterised by H<sub>2</sub>O-saturated conditions, as the peak  
 242 assemblage would not have formed if undersaturated and only requires ~1 mol. % H<sub>2</sub>O to reach  
 243 saturation (Fig. S1). Furthermore, the inferred prograde  $P$ - $T$  path passes through talc-bearing  
 244 fields (orange line, Fig. 6), consistent with its presence as inclusions in garnet (Fig. 2d), and  
 245 the trajectory of the path enters the peak field at ~27 kbar, in excellent agreement with the  
 246 upper range of measured phengite Si pfu (3.50; Table 2). More nuanced modelling is not applied  
 247 as the conclusions of this study do not depend upon the absolute shape of the prograde  $P$ - $T$   
 248 path.

249 To constrain the peak temperature, the Ti content of rutile grains included in garnet rims  
 250 (Table S1) is used, following the calibration of Watson et al. (2006). This analysis yielded  
 251 temperatures of 628–669 °C (red text, Fig. 9), with the upper bound considered as the best  
 252 estimate of peak temperature conditions, to account for possible temperature increases during  
 253 growth of the enveloping garnet rim. Overall, peak conditions of  $\sim 27 \pm 1$  kbar and  $670 \pm 50$  °C  
 254 are suggested, with errors of  $\pm 1$  kbar and 50 °C applied as a minimum estimate of uncertainty  
 255 ( $2\sigma$ ; Powell and Holland, 2008; Palin et al., 2016). This result is within reasonable error of a  
 256 previous estimate of 27 kbar and 730 °C for the Sumdo eclogite locality (purple data, Fig. 9;  
 257 Yang et al., 2009). An exhumation path is suggested for sample nt2 (grey arrow, Fig. 9) that  
 258 takes into account petrographic observations of the retrograde growth of calcic amphibole and  
 259 epidote, and the sequential growth of ilmenite and titanite after rutile (Fig. 2g). Again the path  
 260 is qualitative as H<sub>2</sub>O-undersaturated conditions would have prevailed during decompression  
 261 (hence high-pressure assemblages are preserved), but it serves to illustrate that a hairpin-style  
 262 subduction–exhumation path is plausible for sample nt2.

## 263 6. Discussion

### 264 6.1. Metamorphism of the Sumdo eclogite locality

265 *In situ* geochronological analysis of zircon in sample nt2 yielded an age of  $273.6 \pm 2.8$  Ma (Fig. 5).  
 266 Rock-forming mineral inclusions within zircon hosts are shown to be stable in the  $P$ - $T$  limits

267 of 15.5–16.5 kbar and 500–560 °C (Fig. 7), which implies that zircon growth occurred during  
 268 prograde metamorphism (subduction) leading to peak conditions of  $27 \pm 1$  kbar and  $670 \pm 50$  °C  
 269 (Fig. 9). Based on the spongy, inclusion-rich nature of the zircons and their diffuse ‘mosaic-type’  
 270 CL patterns (Fig. 4), zircon growth is suggested to have occurred by recrystallisation of protolith  
 271 magmatic zircon by subsolidus dissolution–precipitation under the influence of metamorphic  
 272 fluids (Rubatto et al., 2008). Previously, HP metamorphic conditions of  $\sim 2.7$  GPa and 730 °C  
 273 at  $262 \pm 5$  Ma (U–Pb zircon) have been reported for the Sumdo eclogite locality by Yang et al.  
 274 (2009), with inclusions of rutile, omphacite and garnet within the zircon linking the zircon age  
 275 to the timing of eclogite-facies metamorphism. The results of this study are in good agreement  
 276 with those of Yang et al. (2009), as the peak  $P$ – $T$  conditions overlap, and their slightly younger  
 277 U–Pb age may represent a peak or retrograde age, as the documented inclusion suite (rutile,  
 278 omphacite and garnet) is stable over a wide region of eclogite-facies  $P$ – $T$  space (e.g. the green  
 279 shaded region on Fig. 9 for sample nt2)

## 280 6.2. Metamorphism of the Sumdo complex

281 The Sumdo complex is thought to represent the trace of either an ocean basin or a back-arc  
 282 basin that opened during the Carboniferous, with metamorphism of the complex interpreted  
 283 to have occurred in a subduction zone that was established during the early Permian (Yang  
 284 et al., 2009), prior to accretion of the north and south Lhasa terranes and exhumation along the  
 285 Luobadui–Milashan suture (Fig. 1a) at *c.* 241–224 Ma (Ms Ar–Ar; Li et al., 2012). Although  
 286 the  $P$ – $T$ –time data reported from different eclogite exposures in the Sumdo complex are highly  
 287 variable (Table 4), analysis of the age distribution indicates that eclogite-facies metamorphism  
 288 occurred in two time periods (orange shading, Fig. 10): at *c.* 267–257 Ma (Yang et al., 2009;  
 289 Cheng et al., 2012), and *c.* 242–225 Ma (Zeng et al., 2009; Cheng et al., 2015). Notably, these  
 290 two age intervals coincide with the limits of the subduction zone lifecycle: soon after formation  
 291 of the subduction zone sometime in the early Permian (precise age unknown), and coincident  
 292 with accretion of the north and south Lhasa terranes in the mid-Triassic (blue shading, Fig. 10).  
 293 The older age bracket is also associated with hotter peak conditions of 620–790 °C (including  
 294 this study), compared with 465–720 °C in the younger age bracket. These features indicate  
 295 enhanced eclogite exhumation potential at either end of a subduction zone lifecycle, possibly



because during these intervals buoyant, attenuated continental margins are most likely to be involved with the subduction process (e.g. Agard et al., 2009). This scenario is consistent with the dominance of continental clastic material in the Sumdo complex (Fig. 1b). Further work is required to delineate the lateral extent of the complex and decipher its tectonic setting (marginal to an ocean basin or back-arc basin), but given the lack of arc volcanics to the south of an appropriate age, there is currently no evidence that the Sumdo complex is related to a back-arc setting.

### 6.3. Zircon crystallisation

Zircon is one of the most important and ubiquitous chronometric minerals available to the geological community (e.g. Corfu, 2003); however, it is often difficult to reliably interpret the timing of growth of dated grains with respect to the metamorphic history of the host sample. Commonly it is noted that zircon crystallisation in metabasic rocks occurs at eclogite-facies conditions, usually based on the identification of high pressure inclusions in the zircon grains, such as garnet, omphacite or coesite (e.g. Parrish et al., 2006; Yang et al., 2009), or inferred from rare earth element analysis, which typically indicates garnet-present but plagioclase-absent parageneses during zircon crystallisation (e.g. Rubatto and Hermann, 2003; Baldwin et al., 2004). Whilst these arguments are robust, the broad  $P$ - $T$  range over which eclogite-facies mineral assemblages stabilise means that this inference is quantitatively relatively vague. Phase equilibria modelling offers the potential to provide constraints on a sample-specific basis. For example, in sample nt2, garnet and clinopyroxene are both predicted to be stable in plagioclase-free assemblages throughout the suggested  $P$ - $T$  loop above  $\sim 11.5$  kbar (green shaded region, Fig. 9), indicating such constraints permit zircon growth over a broad range of possible prograde, peak and retrograde  $P$ - $T$  conditions.

Phase equilibria in metabasic lithologies are commonly characterised by high-variance, moderately anhydrous assemblages at high-grade conditions (e.g. Powell and Holland, 2008; St-Onge et al., 2013; Weller et al., 2015b), over which changing  $P$ - $T$  conditions are accommodated mostly by changing phase compositions rather than new mineral growth and/or recrystallisation. Consequently the nucleation and growth of zircon at peak conditions is less likely than at

324 lower grade (prograde or retrograde) conditions. Several studies have noted links between zircon  
 325 growth and transitions between ilmenite, titanite and rutile, as these phases contain some of  
 326 the highest concentrations of Zr of common rock-forming minerals, such that reactions amongst  
 327 the titanium-bearing phases can cause significant redistribution of Zr in a given sample (Bea  
 328 et al., 2006). While several textural studies have proposed that subsolidus metamorphic zircon  
 329 crystallisation can be precipitated by prograde rutile growth (e.g. Bingen et al., 2001; Beckman  
 330 et al., 2014), Kohn et al. (2015) used mass balance considerations of the zirconium budget in  
 331 metabasites to suggest that most zircon growth should be retrograde, as the breakdown of ru-  
 332 tile to ilmenite and/or titanite is a Zr source. Analysis of the Zr contents of ilmenite, titanite  
 333 and rutile in this sample (inset, Fig. 9) is consistent with the notion that prograde–retrograde  
 334 transitions would represent a Zr source, but such mass balance analysis does not consider the  
 335 contribution that could be made by primary igneous zircon, which is the Zr source in this case.  
 336 Ultimately, reports of zircon growth in eclogite at prograde (e.g. Bingen et al., 2001; St-Onge  
 337 et al., 2013; Beckman et al., 2014), peak (e.g. Rubatto and Hermann, 2003; Baldwin et al.,  
 338 2004; Parrish et al., 2006; Yang et al., 2009; St-Onge et al., 2013) and/or retrograde (e.g. Leech  
 339 et al., 2007; Kohn et al., 2015) conditions suggests that multiple zircon growth mechanisms are  
 340 possible, and careful *in situ* analysis is required to determine what a given age relates to for a  
 341 given sample, as a metamorphic zircon panacea is unlikely to be found.

## 342 **7. Acknowledgements**

343 The authors acknowledge a Natural Environment Research Council (NERC) postgraduate grant  
 344 to O. Weller, reference number NE/I528485/1, with this work forming part of the PhD research  
 345 for the first author. The following people are thanked: S.-L. Chung (NTU) for XRF data,  
 346 J. Hyde (Oxford) for thin section preparation, P. Hunt (GSC) and N. Charnley (Oxford) for  
 347 SEM support, B. Joy (Queen’s) for EMP analysis, T. Pestaj (GSC) for SHRIMP support, the  
 348 Hard Rock Group at Oxford for convivial discussion, B. Davis (GSC) and R. Parrish (BGS)  
 349 for early manuscript comments and S. Wallis (Nagoya) and one anonymous reviewer for highly  
 350 constructive and informative comments. O. Weller’s and N. Rayner’s SHRIMP work and M.  
 351 St-Onge’s travel and research were all funded by the Earth Sciences Sector, Natural Resources

352 Canada. This is Earth Sciences Sector contribution no. 20150104.

## 353 **References**

354 Agard, P., Yamato, P., Jolivet, L., Burov, E., 2009. Exhumation of oceanic blueschists and  
355 eclogites in subduction zones: Timing and mechanisms. *Earth-Science Reviews* 92, 53–79.  
356 doi:10.1016/j.earscirev.2008.11.002.

357 Baldwin, S.L., Monteleone, B.D., Webb, L.E., Fitzgerald, P.G., Grove, M., Hill, E.J., 2004.  
358 Pliocene eclogite exhumation at plate tectonic rates in eastern Papua New Guinea. *Nature*  
359 431, 263–267. doi:10.1038/nature02846.

360 Bea, F., Montero, P., Ortega, M., 2006. A LA–ICP–MS evaluation of Zr reservoirs in com-  
361 mon crustal rocks: Implications for Zr and Hf geochemistry, and zircon-forming processes.  
362 *Canadian Mineralogist* 44, 693–714. doi:10.2113/gscanmin.44.3.693.

363 Beckman, V., Moller, C., Soderlund, U., Corfu, F., Pallon, J., Chamberlain, K.R., 2014. Meta-  
364 morphic zircon formation at the transition from gabbro to eclogite in Trollheimen-Surnadalen,  
365 Norwegian Caledonides. *Geological Society, London, Special Publications* 390, 403–424.  
366 doi:10.1144/SP390.26.

367 Bingen, B., Austrheim, H., Whitehouse, M., 2001. Ilmenite as a source for zirconium  
368 during high-grade metamorphism? Textural evidence from the Caledonides of western  
369 Norway and implications for zircon geochronology. *Journal Of Petrology* 42, 355–375.  
370 doi:10.1093/petrology/42.2.355.

371 Black, L.P., Kamo, S.L., Allen, C.M., Davis, D.W., Aleinikoff, J.N., Valley, J.W., Mundil, R.,  
372 Campbell, I.H., Korsch, R.J., Williams, I.S., Foudoulis, C., 2004. Improved  $^{206}\text{Pb}/^{238}\text{U}$  mi-  
373 croprobe geochronology by the monitoring of a trace-element-related matrix effect; SHRIMP,  
374 ID–TIMS, ELA–ICP–MS and oxygen isotope documentation for a series of zircon standards.  
375 *Chemical Geology* 205, 115–140. doi:10.1016/j.chemgeo.2004.01.003.

376 Cheng, H., Liu, Y., Vervoort, J.D., Lu, H., 2015. Combined U–Pb, Lu–Hf, Sm–Nd and  
377 Ar–Ar multichronometric dating on the Bailang eclogite constrains the closure timing of

the Paleo-Tethys Ocean in the Lhasa terrane, Tibet. *Gondwana Research* 28, 1482–1499.  
doi:10.1016/j.gr.2014.09.017.

Cheng, H., Zhang, C., Vervoort, J.D., Lu, H., Wang, C., Cao, D., 2012. Zircon U–Pb and  
garnet Lu–Hf geochronology of eclogites from the Lhasa Block, Tibet. *Lithos* 155, 341–359.  
doi:10.1016/j.lithos.2012.09.011.

Clarke, G.L., Powell, R., Fitzherbert, J.A., 2006. The lawsonite paradox: a comparison of field  
evidence and mineral equilibria modelling. *Journal of Metamorphic Geology* 24, 715–725.  
doi:10.1111/j.1525-1314.2006.00664.x.

Coggon, R., Holland, T.J.B., 2002. Mixing properties of phengitic micas and revised garnet–  
phengite thermobarometers. *Journal of Metamorphic Geology* 20, 683–696.

Corfu, F., 2003. Atlas of Zircon Textures. *Reviews in Mineralogy and Geochemistry* 53, 469–500.  
doi:10.2113/0530469.

Diener, J.F.A., Powell, R., 2010. Influence of ferric iron on the stability of mineral assemblages.  
*Journal of Metamorphic Geology* 28, 599–613. doi:10.1111/j.1525-1314.2010.00880.x.

Diener, J.F.A., Powell, R., 2012. Revised activity–composition models for clinopyroxene and am-  
phibole. *Journal of Metamorphic Geology* 30, 131–142. doi:10.1111/j.1525-1314.2011.00959.x.

Dong, X., Zhang, Z., Liu, F., Wang, W., Yu, F., Shen, K., 2011. Zircon U–Pb geochronol-  
ogy of the Nyainqentanglha Group from the Lhasa terrane: New constraints on the  
Triassic orogeny of the south Tibet. *Journal of Asian Earth Sciences* 42, 732–739.  
doi:10.1016/j.jseaes.2011.01.014.

Endo, S., Wallis, S.R., Tsuboi, M., Aoya, M., Uehara, S., 2012. Slow subduc-  
tion and buoyant exhumation of the Sanbagawa eclogite. *Lithos* 146–147, 183–201.  
doi:10.1016/j.lithos.2012.05.010.

Holland, T., Baker, J., Powell, R., 1998. Mixing properties and activity–composition relation-  
ships of chlorites in the system  $\text{MgO–FeO–Al}_2\text{O}_3\text{–SiO}_2\text{–H}_2\text{O}$ . *European Journal of Mineralogy*  
10, 395–406.

- 404 Holland, T.J.B., 2009. AX: a program to calculate activities of mineral end-members from  
405 chemical analyses.
- 406 Holland, T.J.B., Powell, R., 1998. An internally consistent thermodynamic data set for phases  
407 of petrological interest. *Journal of Metamorphic Geology* 16, 309–343. doi:10.1111/j.1525-  
408 1314.1998.00140.x.
- 409 Holland, T.J.B., Powell, R., 2003. Activity–composition relations for phases in petrological  
410 calculations: an asymmetric multicomponent formulation. *Contributions to Mineralogy and  
411 Petrology* 145, 492–501. doi:10.1007/s00410-003-0464-z.
- 412 Kohn, M.J., Corrie, S.L., Markley, C., 2015. The fall and rise of metamorphic zircon. *American  
413 Mineralogist* 100, 897–908. doi:10.2138/am-2015-5064.
- 414 Kohn, M.J., Spear, F.S., 2000. Retrograde net transfer reaction insurance for pressure-  
415 temperature estimates. *Geology* 28, 1127–1130. doi:10.1130/0091-7613(2000)28<1127.
- 416 Leech, M.L., Singh, S., Jain, A.K., 2007. Continuous Metamorphic Zircon Growth and Inter-  
417 pretation of U–Pb SHRIMP Dating: An Example from the Western Himalaya. *International  
418 Geology Review* 49, 313–328. doi:10.2747/0020-6814.49.4.313.
- 419 Li, H., Xu, Z., Yang, J., Tang, Z., 2012. Indosinian Orogenesis in the Lhasa Terrane, Tibet:  
420 New Muscovite  $^{40}\text{Ar}$ – $^{39}\text{Ar}$  Geochronology and Evolutionary Process. *Acta Geologica Sinica*  
421 86, 1116–1127.
- 422 Lin, Y.H., Zhang, Z.M., Dong, X., Xiang, H., Yan, R., 2013. Early Mesozoic metamorphism  
423 and tectonic significance of the eastern segment of the Lhasa terrane, south Tibet. *Journal  
424 of Asian Earth Sciences* 78, 160–183. doi:10.1016/j.jseaes.2013.04.009.
- 425 Ludwig, K., 2003. User’s Manual for Isoplot/Ex rev. 3.00: a Geochronological Toolkit for  
426 Microsoft Excel. Special Publications, 4, Berkeley Geochronology Center, Berkeley. Technical  
427 Report.
- 428 Palin, R., St-Onge, M., Waters, D., Searle, M., Dyck, B., 2014. Phase equilibria modelling of  
429 retrograde amphibole and clinozoisite in mafic eclogite from the Tso Moriri massif, northwest

430 India: constraining the  $P$ - $T$ - $M(\text{H}_2\text{O})$  conditions of exhumation. *Journal of Metamorphic*  
431 *Geology* 32, 675–693. doi:10.1111/jmg.12085.

432 Palin, R.M., Searle, M.P., St-Onge, M.R., Waters, D.J., Roberts, N.M.W., Horstwood, M.S.A.,  
433 Parrish, R.R., Weller, O.M., 2015. Two-stage cooling history of pelitic and semi-pelitic my-  
434 lonite (*sensu lato*) from the Dongjiu-Milin shear zone, northwest flank of the eastern Hi-  
435 malayan syntaxis. *Gondwana Research* 28, 509–530. doi:10.1016/j.gr.2014.07.009.

436 Palin, R.M., Weller, O.M., Waters, D.J., Dyck, B., 2016. Quantifying geological uncertainty  
437 in metamorphic phase equilibria modelling; a Monte Carlo assessment and implications for  
438 tectonic interpretations. *Geoscience Frontiers* (in press). doi:10.1016/j.gsf.2015.08.005.

439 Parrish, R.R., Gough, S., Searle, M.P., Waters, D.J., 2006. Plate velocity exhumation  
440 of ultrahigh-pressure eclogites in the Pakistan Himalaya. *Geology* 34, 989–992.  
441 doi:10.1130/G22796A.1.

442 Powell, R., Holland, T.J.B., 2008. On thermobarometry. *Journal of Metamorphic Geology* 26,  
443 155–179. doi:10.1111/j.1525-1314.2007.00756.x.

444 Rayner, N., Stern, R.A., 2002. Improved sample preparation method for SHRIMP analysis  
445 of delicate mineral grains exposed in thin sections. *Geological Survey of Canada, Current*  
446 *Research* 2002-F10 , 1–3.

447 Roduit, N., 2010. JMicroVision: Image analysis toolbox for measuring and quantifying compo-  
448 nents of high-definition images.

449 Rubatto, D., Hermann, J., 2003. Zircon formation during fluid circulation in eclogites (Mon-  
450 viso, Western Alps): Implications for Zr and Hf budget in subduction zones. *Geochimica et*  
451 *Cosmochimica Acta* 67, 2173–2187. doi:10.1016/S0016-7037(02)01321-2.

452 Rubatto, D., Muntener, O., Barnhoorn, A., Gregory, C., 2008. Dissolution-reprecipitation of  
453 zircon at low-temperature, high-pressure conditions (Lanzo Massif, Italy). *American Miner-*  
454 *alogist* 93, 1519–1529. doi:10.2138/am.2008.2874.

455 St-Onge, M.R., Rayner, N., Palin, R.M., Searle, M.P., Waters, D.J., 2013. Integrated pressure-  
456 temperature-time constraints for the Tso Moriri dome (Northwest India): implications for the

457 burial and exhumation path of UHP units in the western Himalaya. *Journal of Metamorphic*  
458 *Geology* 31, 469–504. doi:10.1111/jmg.12030.

459 Stacey, J.S., Kramers, J.D., 1975. Approximation of Terrestrial Lead Isotope Evolution by a  
460 Two-Stage Model. *Earth and Planetary Science Letters* 26, 207–221.

461 Stern, R.A., 1997. The GSC Sensitive High Resolution Ion Microprobe (SHRIMP): analytical  
462 techniques of zircon U–Th–Pb age determinations and performance evaluation. *Radiogenic*  
463 *Age and Isotopic Studies: Report 10; Geological Survey of Canada, Current Research 1997-F*,  
464 1–31.

465 Stern, R.A., Amelin, Y., 2003. Assessment of errors in SIMS zircon U–Pb geochronology us-  
466 ing a natural zircon standard and NIST SRM 610 glass. *Chemical Geology* 197, 111–142.  
467 doi:10.1016/S0009-2541(02)00320-0.

468 Wang, K.L., Chung, S.L., O'Reilly, S.Y., Sun, S.S., Shinjo, R., Chen, C.H., 2004. Geo-  
469 chemical Constraints for the Genesis of Post-collisional Magmatism and the Geody-  
470 namic Evolution of the Northern Taiwan Region. *Journal of Petrology* 45, 975–1011.  
471 doi:10.1093/petrology/egh001.

472 Waters, D.J., Utting, J., 2016. Inclusion suites in eclogite garnets: unreliable witnesses of  
473 prograde metamorphic history, in: 2nd European Mineralogical Conference Abstracts Volume,  
474 pp. 1–2.

475 Watson, E.B., Wark, D.A., Thomas, J.B., 2006. Crystallization thermometers for zircon and  
476 rutile. *Contributions to Mineralogy and Petrology* 151, 413–433. doi:10.1007/s00410-006-  
477 0068-5.

478 Weller, O.M., St-Onge, M.R., Rayner, N., Searle, M.P., Waters, D.J., 2016. Miocene magmatism  
479 in the Western Nyainqentanglha mountains of southern Tibet: An exhumed bright spot?  
480 *Lithos* 245, 147–160. doi:10.1016/j.lithos.2015.06.024.

481 Weller, O.M., St-Onge, M.R., Searle, M.P., Waters, D.J., Rayner, N., Chen, S., Chung, S.L.,  
482 Palin, R.M., 2015a. Quantifying the  $P$ – $T$ – $t$  conditions of north–south Lhasa terrane accre-

tion: new insight into the pre-Himalayan architecture of the Tibetan plateau. *Journal of Metamorphic Geology* 33, 91–113. doi:10.1111/jmg.12112.

Weller, O.M., St-Onge, M.R., Waters, D.J., Rayner, N., Searle, M.P., Chung, S.L., Palin, R.M., Lee, Y.H., Xu, X., 2013. Quantifying Barrovian metamorphism in the Danba Structural Culmination of eastern Tibet. *Journal of Metamorphic Geology* 31, 909–935. doi:10.1111/jmg.12050.

Weller, O.M., Wallis, S.R., Aoya, M., Nagaya, T., 2015b. Phase equilibria modelling of blueschist and eclogite from the Sanbagawa metamorphic belt of south-west Japan reveals along-strike consistency in tectonothermal architecture. *Journal of Metamorphic Geology* 33, 579–596. doi:10.1111/jmg.12134.

White, R.W., Powell, R., Holland, T.J.B., 2007. Progress relating to calculation of partial melting equilibria for metapelites. *Journal of Metamorphic Geology* 25, 511–527. doi:10.1111/j.1525-1314.2007.00711.x.

White, R.W., Powell, R., Holland, T.J.B., Worley, B.A., 2000. The effect of  $\text{TiO}_2$  and  $\text{Fe}_2\text{O}_3$  on metapelitic assemblages at greenschist and amphibolite facies conditions: mineral equilibria calculations in the system  $\text{K}_2\text{O}$ – $\text{FeO}$ – $\text{MgO}$ – $\text{Al}_2\text{O}_3$ – $\text{SiO}_2$ – $\text{H}_2\text{O}$ – $\text{TiO}_2$ – $\text{Fe}_2\text{O}_3$ . *Journal of Metamorphic Geology* 18, 497–511.

Whitney, D.L., Evans, B.W., 2010. Abbreviations for names of rock-forming minerals. *American Mineralogist* 95, 185–187. doi:10.2138/am.2010.3371.

Yang, J., Xu, Z., Li, Z., Xu, X., Li, T., Ren, Y., Li, H., Chen, S., Robinson, P., 2009. Discovery of an eclogite belt in the Lhasa block, Tibet: A new border for Paleo-Tethys? *Journal of Asian Earth Sciences* 34, 76–89. doi:10.1016/j.jseaes.2008.04.001.

Yin, A., Harrison, T.M., 2000. Geologic evolution of the Himalayan-Tibetan Orogen. *Annual Review of Earth and Planetary Sciences* 28, 211–280.

Zeng, L., Liu, J., Gao, L., Chen, F., Xie, K., 2009. Early Mesozoic High-pressure Metamorphism Within the Lhasa Block, Tibet and Implications for Regional Tectonics. *Earth Science Frontiers* 16, 140–151. doi:10.1016/S1872-5791(08)60079-2.



510 **Supporting Information**

511 Additional Supporting Information may be found in the online version of this article:

512 **Fig. S1.** Sample nt2  $T$ - $M_{H_2O}$  phase equilibria diagram.

513 **Table S1.** Ilmenite, Rutile and Titanite major and trace element data.

Figure 1: Field setting. a) Tectonic map of the Tibetan plateau. Yellow star shows study region. The lateral trace of the Luobadui-Milashan suture is primarily based on the distribution of Permian arc-related andesite (not shown) in the north Lhasa terrane (Yang et al., 2009). Abbreviations: MMT = Main Mantle Thrust, K'koram = Karakoram. Modified after Palin et al. (2015). b) Geological map of the Sumdo area. Sample nt2 was collected from the Sumdo eclogite locality. Modified after Cheng et al. (2015).

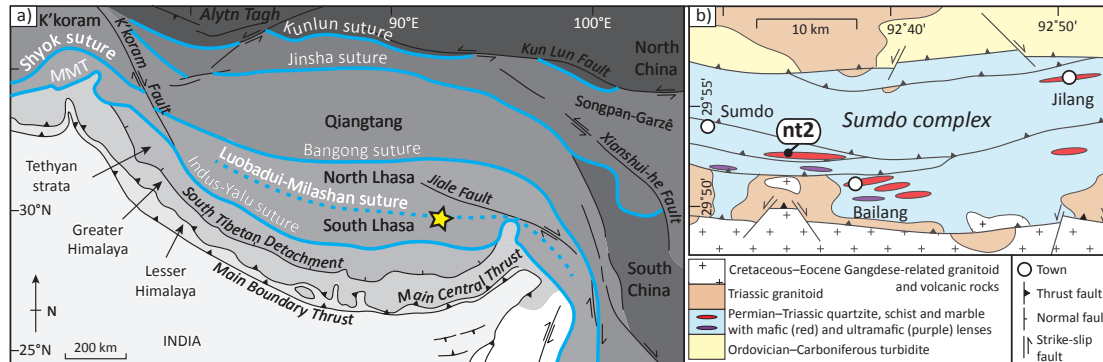


Figure 2: Sample nt2 petrography. a) Field photograph of an eclogite boudin within quartzite at the Sumdo eclogite locality. The rim of the boudin is composed of garnet amphibolite. Geologist for scale is 1.8 m tall. b) Plane-polarised light (PPL) photomicrograph of sample nt2 showing a medium-coarse grain size. c) PPL photomicrograph of sample nt2 showing fractured garnet grains with inclusion-rich interiors and inclusion-poor rims. d) Back-scattered electron (BSE) image of a garnet porphyroblast. Inset: close-up of garnet inclusions. e) BSE image showing amphibole-quartz intergrowths surrounding omphacite that grade into amphibole plates that embay into garnet grains. f) BSE image showing titanite in garnet cores and rutile inclusions in garnet rims. g) BSE image showing matrix rutile and granular ilmenite rimmed by films of titanite.

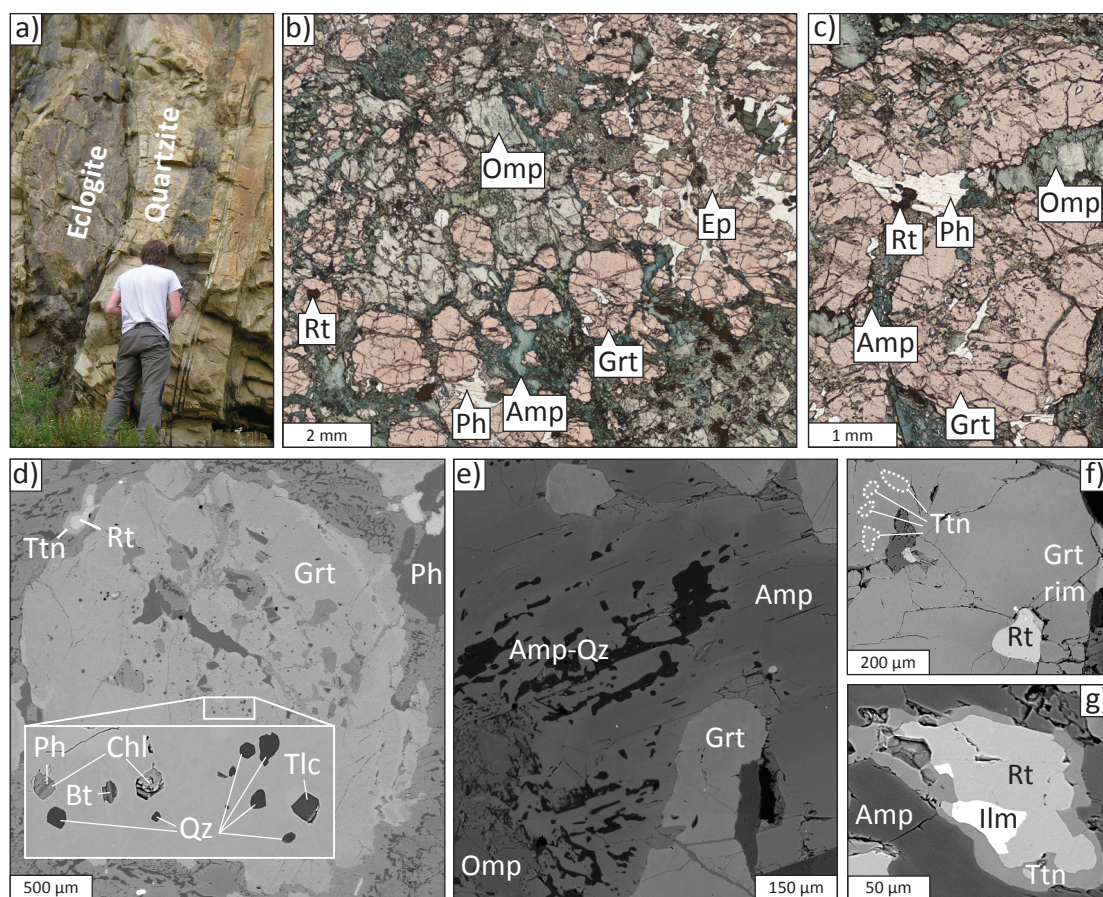


Figure 3: Sample nt2 garnet profile. a) Back-scattered electron image of a euhedral garnet porphyroblast. The white arrow marks the location of the compositional profile shown in (c). (b) X-ray compositional maps for Mg, Ca, Mn and Fe in garnet. Green–blue shading indicates high–low concentrations, but the intensity is not comparable between maps. (c) Compositional profile. Data gaps represent inclusions encountered along each traverse, which were omitted from the line profiles. The stippled region corresponds to where Mn is increasing from core–rim, which is not considered to be representative of prograde growth; see text for discussion.

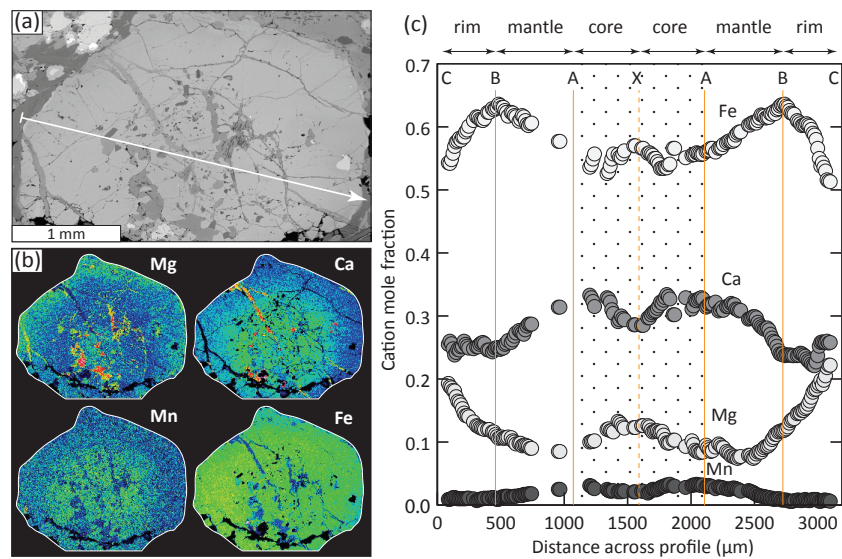


Figure 4: Sample nt2 zircon images. Back-scattered electron (BSE) images of zircon analysed *in situ* (a–d), with BSE (e–h) and cathodoluminescence (i–l) close-ups of the (arrowed) grains. Insets in (e–h) show BSE images of inclusions present in the zircon grains, which were identified using EDS spectra and reproduced in multiple grains. Ion beam pits (white ellipses,  $\sim 12 \mu\text{m}$  diameter) shown for scale. Spot ages ( $1\sigma$  errors) are  $^{207}\text{Pb}$  corrected (Table 3).

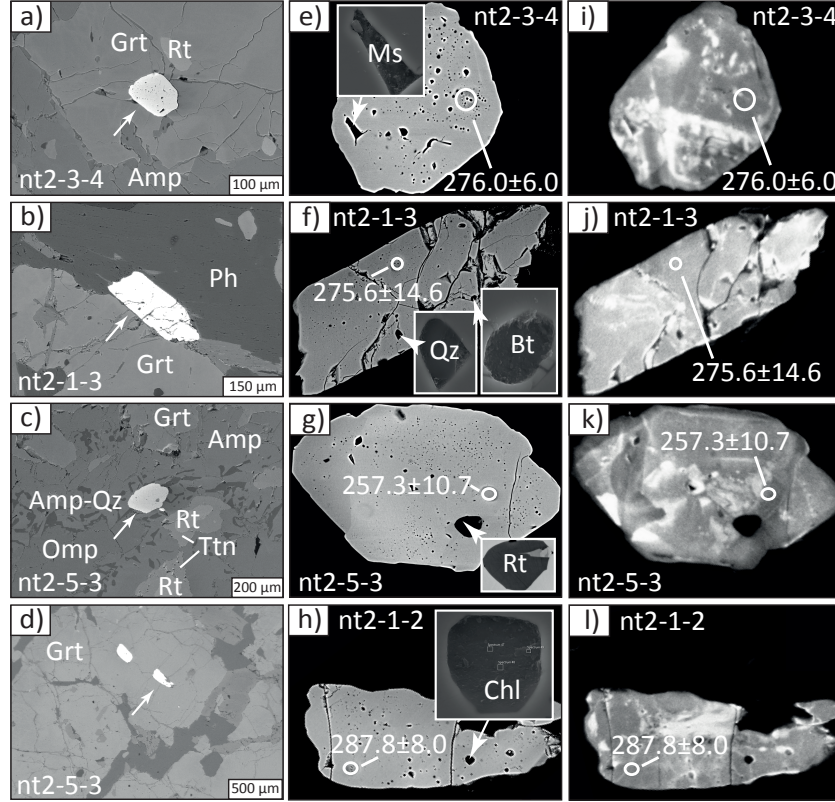
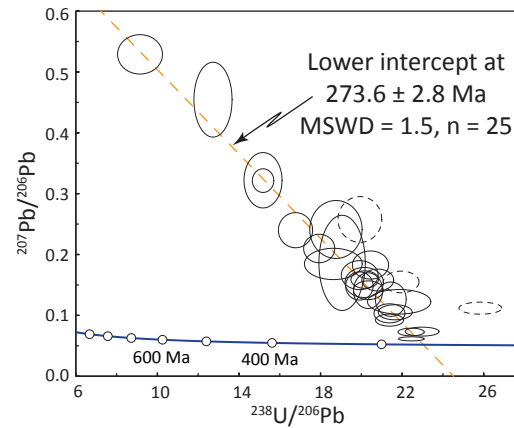


Figure 5: Sample nt2 common-Pb uncorrected Tera-Wasserburg diagram. Error ellipses are 95 % confidence. Common-Pb upper intercept composition (0.852) calculated using a free regression. Dashed ellipses are excluded from the regression due to assumed  $^{206}\text{Pb}$  loss.





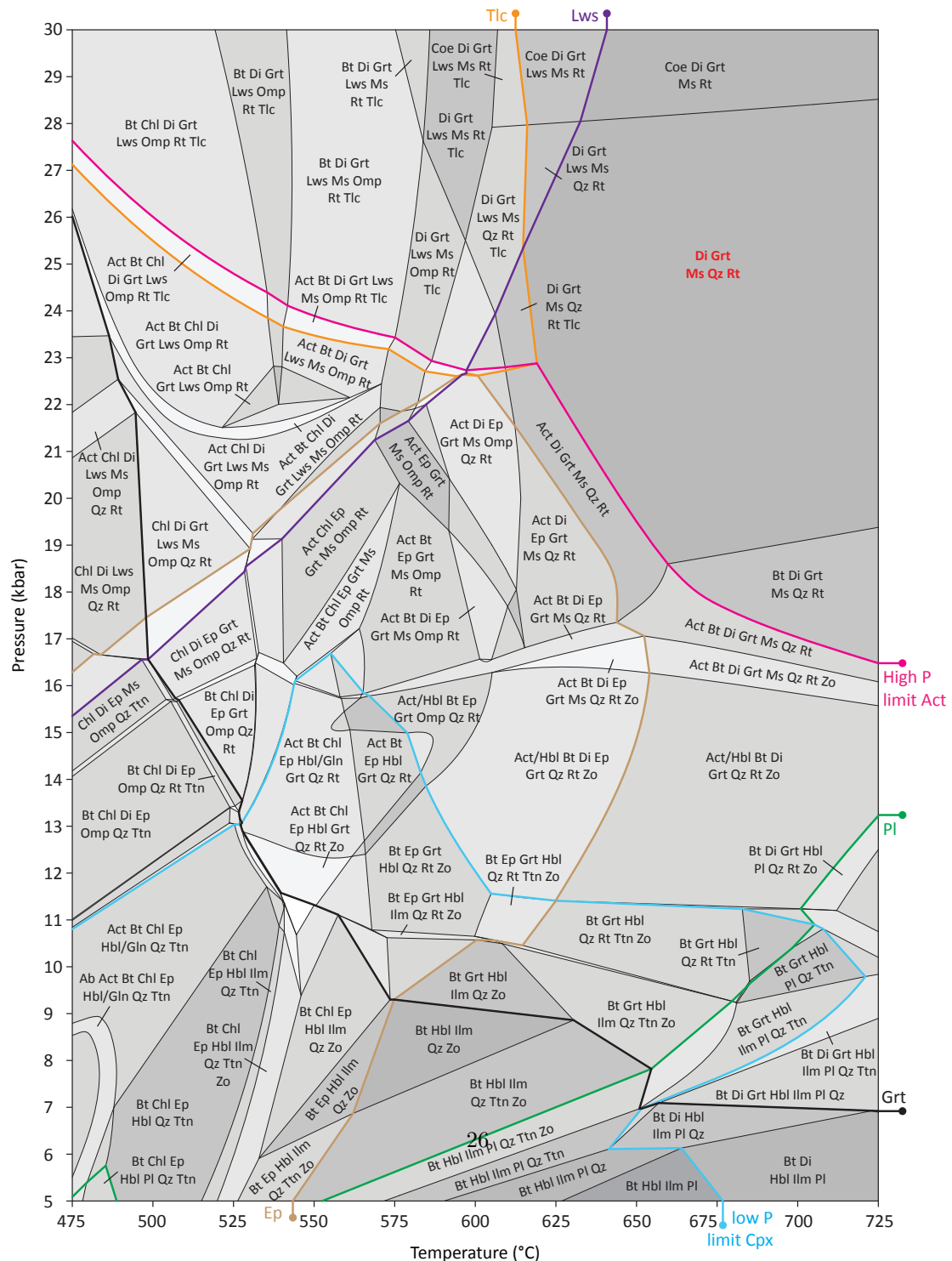


Figure 7: As Fig. 6, but only showing the stability fields of all phases observed as inclusions in zircon. The area where all phases theoretically co-exist is shaded orange.

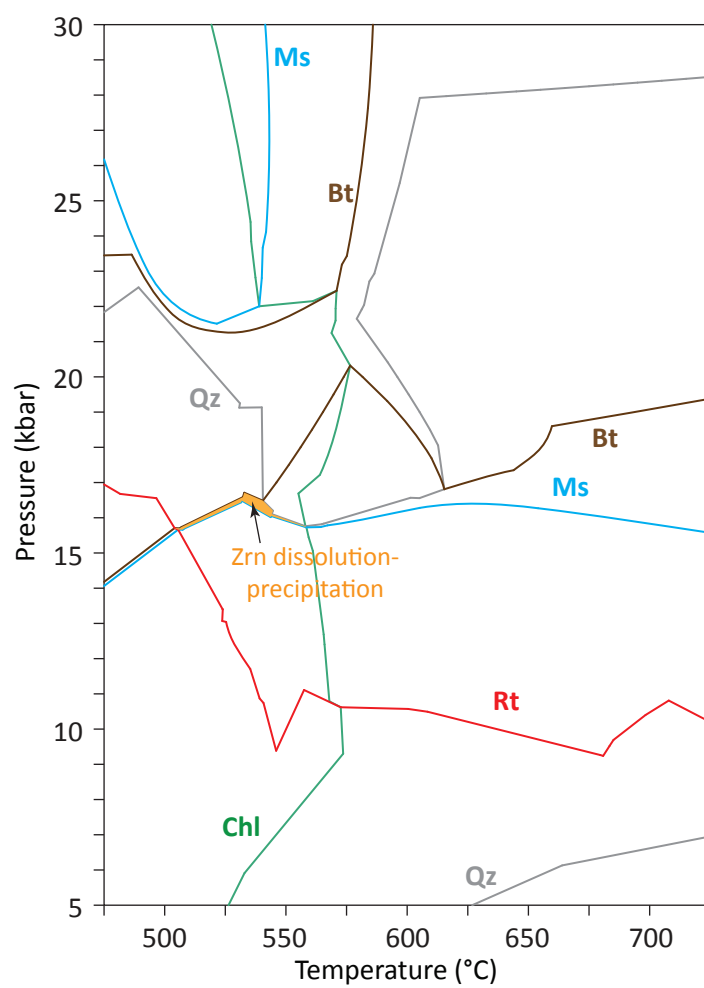


Figure 8: As Fig. 6 but showing selected compositional isopleths. Diopside and muscovite isopleths and additional garnet isopleths are only shown in the peak field for clarity. Labels A and B correspond to the location of isopleth intersections shown on Fig. 3b (renormalised without Mn). As the phase diagram does not account for garnet cation fractionation, these locations are only qualitative. Grt rim Zr(Rt) T refers to the range of temperatures calculated using the Zr content of rutile located in garnet rims (Table S1). Orange shaded region is from Fig. 7. An estimate of peak conditions is shown as a white circle with associated uncertainties of  $\pm 1$  kbar and  $\pm 50$  °C.

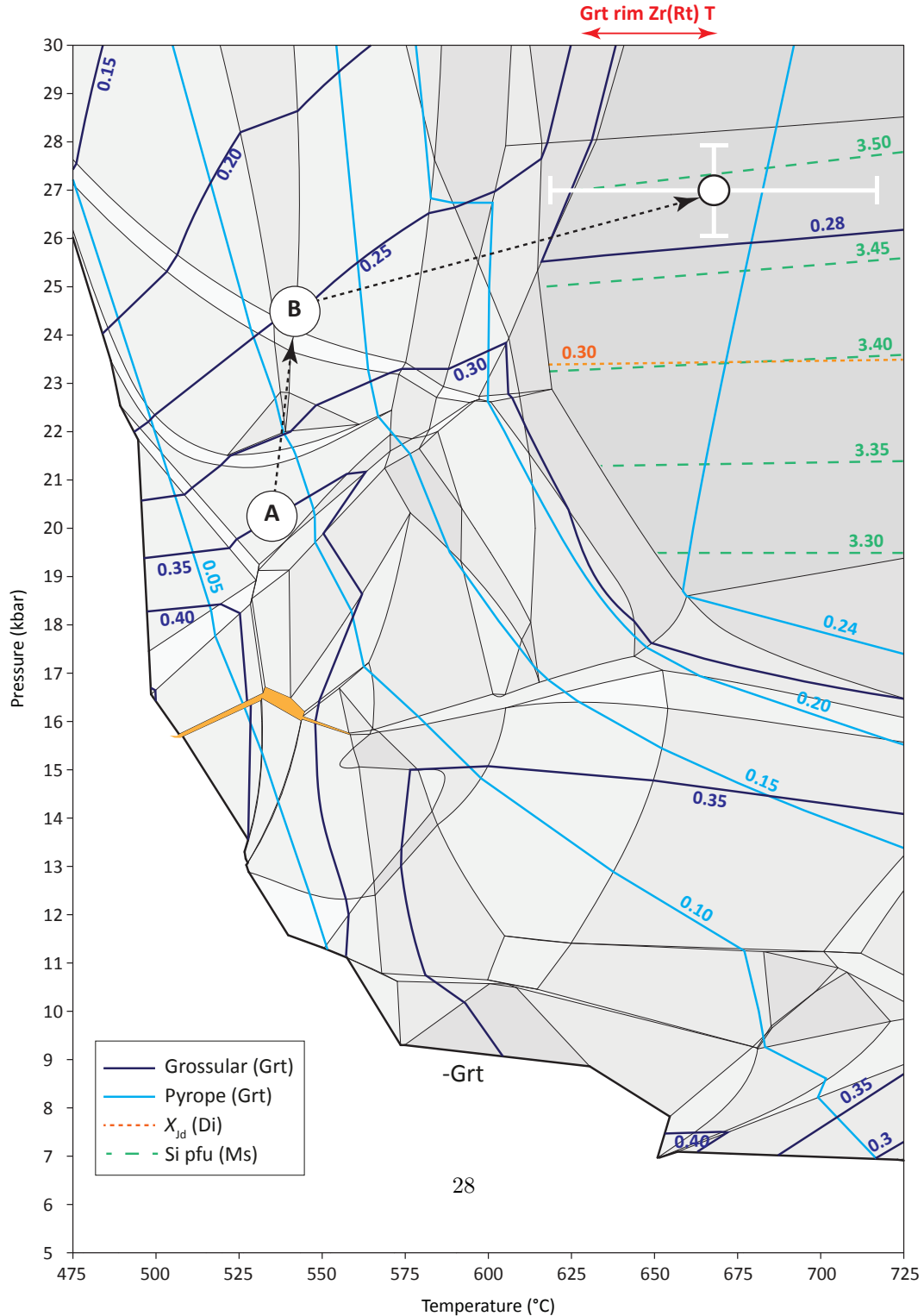




Figure 9: Amalgamated results. The conditions of prograde zircon dissolution–precipitation (Fig. 7) and peak metamorphism (Fig. 8) are quantitative, whereas the suggested  $P$ – $T$  path is qualitative. Ilmenite, rutile and titanite stability fields are highlighted from Fig. 6, and the inset shows their respective Zr contents (\*presented as the average of the values given in Table S1). The green shaded region represents where garnet and clinopyroxene co-exist in the absence of plagioclase for the sample nt2 bulk composition (Fig. 6); see text for discussion.

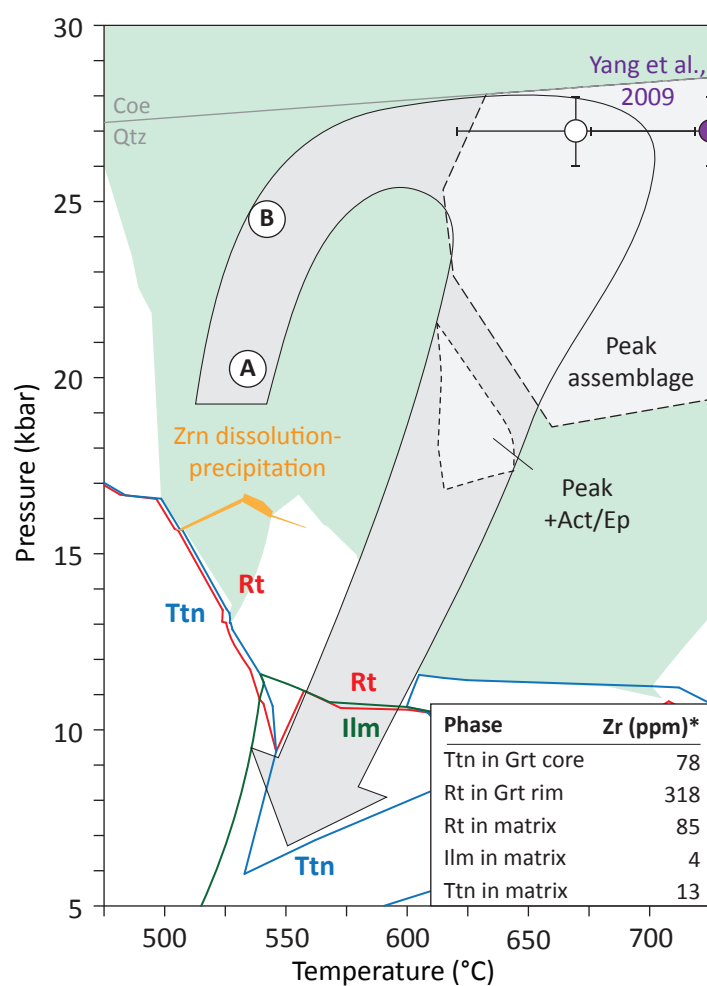


Figure 10: Temperature–time plot of the Sumdo complex. Evidence for eclogite-facies metamorphism in the Sumdo complex occurred in two time periods during the subduction zone lifecycle (orange shading): soon after formation of the subduction zone, and coincident with the onset of continental convergence. The older age bracket is also associated with hotter peak conditions. These features suggest discontinuous eclogite exhumation at either end of a subduction zone lifecycle. All data points are detailed in Table 4. \*This study. ? = location unknown.

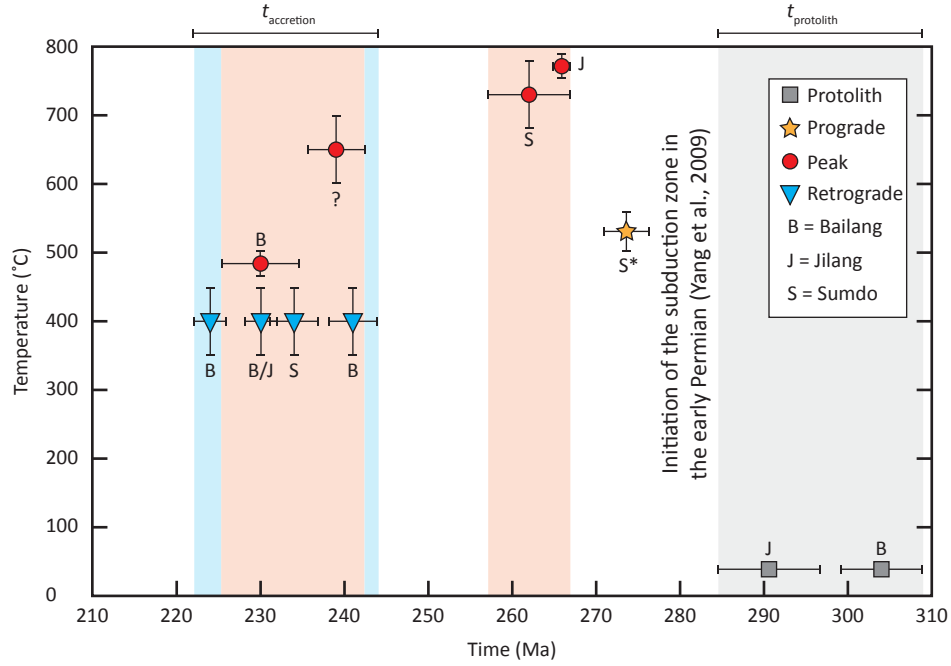


Table 1: Sample nt2 X-ray fluorescence data (wt. %).

SiO <sub>2</sub>	TiO <sub>2</sub>	Al <sub>2</sub> O <sub>3</sub>	Fe <sub>2</sub> O <sub>3</sub>	MnO	MgO	CaO	Na <sub>2</sub> O	K <sub>2</sub> O	P <sub>2</sub> O <sub>5</sub>	Total
43.06	2.86	15.13	17.01	0.24	6.96	11.39	1.28	0.75	0.29	98.97

Table 2: Representative sample nt2 SEM-EDS data. As electron-microprobe analysis cannot discriminate between  $\text{Fe}^{2+}$  and  $\text{Fe}^{3+}$ , all Fe in wt. % analyses is given as FeO. Cation totals were calculated using AX (Holland, 2009), which provides an estimate of  $X_{\text{Fe}^{3+}}$  where stoichiometric criteria can be applied.  $X_{\text{Mg}} = \text{Mg}/(\text{Mg} + \text{Fe}^{2+})$ ;  $X_{\text{Fe}^{3+}} = \text{Fe}^{3+}/(\text{Fe}^{2+} + \text{Fe}^{3+})$ ;  $X_{\text{Jd}} = \text{Na}/(\text{Na} + \text{Ca})$ ;  $X_{\text{Ps}} = \text{Fe}^{3+}/(\text{Fe}^{3+} + \text{Al})$ ;  $\text{Sps} = \text{Mn}/(\text{Fe}^{2+} + \text{Mg} + \text{Ca} + \text{Mn})$ ;  $\text{Prp} = \text{Mg}/(\text{Fe}^{2+} + \text{Mg} + \text{Ca} + \text{Mn})$ ;  $\text{Grs} = \text{Ca}/(\text{Fe}^{2+} + \text{Mg} + \text{Ca} + \text{Mn})$ ;  $\text{Alm} = \text{Fe}^{2+}/(\text{Fe}^{2+} + \text{Mg} + \text{Ca} + \text{Mn})$ .

Mineral	Prograde phases			Peak phases						Retrograde phases				
	Chl	Ph	Tlc	Grt	Grt	Omp	Omp	Ph	Ph	Act	Prg	Ed	Chl	Ep
Location	Grt incl.	Grt incl.	Grt incl.	core	rim	core	rim	core	rim	plate core	plate rim	sponge	Grt cracks	matrix
SiO <sub>2</sub>	26.16	50.90	60.27	37.73	37.98	54.49	53.43	51.37	50.64	50.86	41.83	45.24	24.93	37.55
TiO <sub>2</sub>	0.01	0.16	0.00	0.17	0.10	0.08	0.21	0.39	0.46	0.11	0.33	0.28	0.04	0.12
Al <sub>2</sub> O <sub>3</sub>	19.63	25.05	0.36	20.60	21.11	5.15	5.84	24.22	25.48	5.54	15.04	9.41	18.49	25.61
FeO	23.41	3.36	6.32	24.85	25.37	6.03	8.53	3.48	4.13	12.59	18.57	15.20	32.83	9.54
MnO	0.14	0.01	0.04	1.39	0.40	0.03	0.04	0.01	0.03	0.12	0.12	0.07	0.60	0.07
MgO	16.97	3.80	27.12	2.90	5.67	12.08	10.14	3.73	3.44	13.84	8.07	11.31	9.79	0.02
CaO	0.09	0.04	0.16	12.36	9.06	18.57	17.59	0.03	0.25	9.30	9.91	10.12	0.09	23.57
Na <sub>2</sub> O	0.01	0.43	0.02	0.00	0.00	3.42	4.04	0.08	0.20	2.16	3.16	2.35	0.01	0.00
K <sub>2</sub> O	0.01	10.39	0.11	0.00	0.00	0.00	0.00	10.36	10.20	0.12	1.04	0.53	0.01	0.02
Total	86.45	94.14	94.39	100.00	99.68	99.85	99.81	93.67	94.83	94.64	98.07	94.53	86.78	96.49
Si	2.77	3.46	3.96	2.97	2.96	1.98	1.95	3.50	3.42	7.50	6.26	6.87	2.79	5.95
Ti	0.00	0.01	0.00	0.01	0.01	0.00	0.01	0.02	0.02	0.01	0.04	0.03	0.00	0.01
Al	2.45	2.01	0.03	1.91	1.94	0.22	0.25	1.95	2.03	0.96	2.65	1.68	2.44	4.78
Fe <sup>3+</sup>	0.01	0.00	0.04	0.13	0.13	0.06	0.12	0.00	0.05	0.28	0.30	0.28	0.00	1.22
Fe <sup>2+</sup>	2.06	0.19	0.31	1.50	1.52	0.12	0.14	0.20	0.18	1.27	2.03	1.65	3.07	0.05
Mn	0.01	0.00	0.00	0.09	0.03	0.00	0.00	0.00	0.00	0.01	0.02	0.01	0.06	0.01
Mg	2.68	0.39	2.66	0.34	0.66	0.65	0.55	0.38	0.35	3.04	1.80	2.56	1.63	0.00
Ca	0.01	0.00	0.01	1.04	0.76	0.72	0.69	0.00	0.02	1.47	1.59	1.65	0.01	4.00
Na	0.00	0.06	0.00	0.00	0.00	0.24	0.29	0.01	0.03	0.62	0.92	0.69	0.00	0.00
K	0.00	0.90	0.01	0.00	0.00	0.00	0.00	0.90	0.88	0.02	0.20	0.10	0.00	0.00
Sum	10.00	7.01	7.02	8.00	8.00	4.00	4.00	6.96	6.97	15.19	15.79	15.52	10.00	16.03
Oxygens	14	11	11	12	12	6	6	11	11	23	23	23	14	25
X <sub>Mg</sub>	0.56	0.67	0.89	0.18	0.30	0.84	0.79	0.66	0.65	0.71	0.47	0.61	0.35	-
X <sub>Fe<sup>3+</sup></sub>	0.00	0.00	0.10	0.08	0.08	0.33	0.45	0.00	0.21	0.18	0.13	0.14	0.00	0.96
X <sub>Jd</sub>	-	-	-	-	-	0.25	0.29	-	-	-	-	-	-	-
X <sub>Ps</sub>	-	-	-	-	-	-	-	-	-	-	-	-	-	0.20
Sps	-	-	-	0.03	0.01	-	-	-	-	-	-	-	-	-
Prp	-	-	-	0.11	0.22	-	-	-	-	-	-	-	-	-
Grs	-	-	-	0.35	0.26	-	-	-	-	-	-	-	-	-
Alm	-	-	-	0.50	0.51	-	-	-	-	-	-	-	-	-

Table 3: Sample nt2 U–Pb zircon data. The column ‘Petrographic position’ lists the phases in contact with the analysed zircon grain.

Analysis	Petro. position	U (ppm)	Th (ppm)	<sup>232</sup> Th/ <sup>238</sup> U	Yb (ppm)	Hf (ppm)	<sup>206</sup> Pb* (ppm)	<sup>204</sup> Pb/ <sup>206</sup> Pb	± f(206) <sup>207</sup> (%)	<sup>208</sup> Pb* <sup>206</sup> Pb*	± (%)	Ratios										Ages (Ma)							
												Uncorrected					204Pb corr.					204Pb corr.				204Pb corr.			
												<sup>238</sup> U/ <sup>206</sup> Pb	± (%)	<sup>207</sup> Pb/ <sup>206</sup> Pb	± (%)	Error	<sup>207</sup> Pb* <sup>235</sup> U	± (%)	<sup>206</sup> Pb* <sup>238</sup> U	± (%)	corr.	<sup>206</sup> Pb/ <sup>238</sup> U	± (%)	<sup>206</sup> Pb/ <sup>238</sup> U	± (%)	<sup>206</sup> Pb/ <sup>238</sup> U	± (%)	<sup>206</sup> Pb/ <sup>238</sup> U	± (%)
nt2-1-1.1	Grt mid	26	10	0.39	475	10402	0.8	1.8E-2	20	33.09	-0.31	11.8	17.9	1.7	0.210	4.6	0.560	32.5	0.0373	10.1	0.312	236.2	23.5	282.5	6.4				
nt2-1-2.1	Grt mid	22	7	0.32	301	10271	0.8	1.8E-2	33	33.10	-0.19	12.2	16.8	2.0	0.240	4.9	0.351	140.6	0.0399	16.6	0.118	252.1	41.0	287.8	8.0				
nt2-1-3.1	Grt rim-Ph	37	15	0.42	653	9514	1.5	7.1E-3	14	12.95	0.21	18.5	19.1	2.4	0.186	17.2	0.547	46.4	0.0457	3.2	0.070	288.0	9.1	275.6	14.4				
nt2-1-4.1	Rt-Ttn	37	10	0.28	178	11668	1.5	1.8E-3	203	3.21	0.29	7.0	20.8	1.5	0.158	4.6	0.866	36.8	0.0465	6.9	0.187	293.1	19.8	263.2	4.8				
nt2-1-8.1	Omp	9	0	0.03	89	11037	0.4	1.4E-2	20	25.36	0.27	8.5	15.2	2.5	0.322	5.8	0.960	38.5	0.0492	7.1	0.185	309.4	21.5	275.5	11.7				
nt2-1-9.1	Grt mid-Ph	98	24	0.25	163	11255	3.0	4.9E-3	38	8.92	0.04	5.7	25.8	1.7	0.112	3.6	0.191	77.1	0.0353	4.0	0.052	223.3	8.9	226.4	3.9				
nt2-1-9.2	Grt mid-Ph	60	25	0.42	216	10908	2.2	6.9E-3	23	12.70	0.14	5.3	20.2	1.4	0.159	3.7	0.344	47.7	0.0433	3.6	0.076	273.2	9.6	271.2	4.3				
nt2-3-4.1	Grt rim	49	30	0.64	503	9226	2.0	1.5E-3	32	2.65	0.34	5.9	20.3	1.4	0.141	8.5	0.800	11.6	0.0479	1.7	0.145	301.5	5.0	276.0	6.0				
nt2-3-6.1	Amp-Ttn	106	38	0.37	240	13455	3.9	8.4E-4	21	1.54	0.13	6.3	23.0	1.5	0.073	4.1	0.361	6.7	0.0428	1.5	0.227	270.5	4.0	267.3	4.0				
nt2-3-7.1	Amp-Qz	72	35	0.50	943	10649	2.7	3.2E-3	30	5.91	0.16	5.8	21.4	1.3	0.092	4.4	0.269	35.5	0.0440	2.3	0.064	277.6	6.2	280.2	3.9				
nt2-3-11.1	Grt core-Rt	23	8	0.36	381	10306	0.7	1.5E-2	22	28.17	-0.23	7.6	20.4	1.8	0.183	5.2	0.391	43.4	0.0351	8.9	0.206	222.6	19.5	258.4	5.8				
nt2-3-11.2	Grt core-Rt	39	11	0.30	135	10470	1.3	8.5E-3	15	15.55	-0.05	7.8	22.0	1.6	0.155	4.7	0.142	90.4	0.0385	3.2	0.035	243.3	7.6	250.6	4.8				
nt2-3-11.3	Grt core-Rt	20	6	0.31	246	10573	0.8	3.8E-3	21	7.00	0.23	8.9	19.9	1.9	0.168	5.9	0.736	13.9	0.0467	2.4	0.175	294.2	7.0	271.7	6.2				
nt2-3-12.1	Amp-Omp-Rt-Ttn	67	28	0.44	762	10298	2.8	1.8E-3	39	3.22	0.33	4.7	19.9	1.4	0.148	6.4	0.836	11.1	0.0486	1.9	0.172	306.0	5.7	278.8	5.3				
nt2-5-1.1	Ph-Rt-Ttn	140	69	0.51	1176	10701	5.2	3.5E-3	22	6.34	0.19	4.0	21.7	1.6	0.105	4.8	0.325	24.4	0.0432	2.2	0.089	272.9	5.8	272.0	4.6				
nt2-5-2.1	Ph-Ttn	59	24	0.42	445	10974	2.3	1.7E-2	13	31.20	0.04	3.7	15.2	1.4	0.321	2.5	0.499	61.2	0.0453	6.3	0.102	285.7	17.5	275.9	5.6				
nt2-5-3.1	Amp-Qz	8	2	0.28	65	10468	0.3	9.6E-3	29	17.60	0.19	12.4	18.8	2.8	0.241	8.1	0.667	47.4	0.0439	6.8	0.143	277.2	18.4	257.3	10.7				
nt2-5-4.1	Amp-Qz-Ttn	23	8	0.36	364	11416	0.8	4.1E-3	20	7.40	0.13	10.2	21.9	2.9	0.122	6.7	0.372	24.2	0.0424	3.3	0.137	267.5	8.6	263.5	8.1				
nt2-6-4.1	Amp-Grt rim-Qz	49	18	0.39	653	10064	1.7	8.0E-3	24	14.69	-0.01	6.7	21.4	1.4	0.127	9.1	0.008	2466.7	0.0398	4.4	0.002	251.5	10.8	266.9	5.7				
nt2-6-5.1	Amp-Grt rim-Qz	21	7	0.34	202	10459	0.8	4.6E-3	20	8.48	0.24	9.1	20.1	1.9	0.154	6.5	0.559	20.0	0.0454	2.6	0.132	286.5	7.4	273.3	6.5				
nt2-6-6.1	Amp-Grt rim	6	3	0.51	38	10655	0.2	3.1E-2	42	56.41	-0.03	7.6	12.7	3.0	0.454	5.5	0.277	665.9	0.0343	54.9	0.082	217.1	117.2	246.3	17.1				
nt2-6-9.1	Omp	469	736	1.62	1279	8484	17.6	1.0E-3	22	1.91	0.52	3.2	22.5	1.1	0.061	2.2	0.277	8.3	0.0437	1.2	0.147	275.7	3.3	277.6	3.2				
nt2-6-10.1	Amp-Omp-Qz	155	128	0.86	656	9226	5.9	3.2E-4	60	0.59	0.31	3.8	22.4	1.2	0.073	3.5	0.415	5.7	0.0443	1.2	0.213	279.4	3.3	273.9	3.3				
nt2-6-10.2	Amp-Omp-Qz	20	10	0.51	158	10651	0.9	3.2E-3	22	5.85	0.38	8.0	18.6	3.1	0.184	5.7	0.996	10.9	0.0505	3.4	0.312	317.9	10.5	282.6	9.7				
nt2-7-1.1	Amp-Grt rim	22	7	0.35	157	10304	0.9	3.2E-2	12	57.97	-0.21	3.7	9.1	4.9	0.529	2.5	0.513	160.4	0.0459	16.9	0.106	289.5	47.9	279.3	17.6				
nt2-7-1.2	Amp-Grt rim	14	0	0.01	112	16362	0.3	2.4E-2	35	43.49	-0.43	14.3	19.9	2.2	0.258	6.0	0.788	34.8	0.0284	27.0	0.777	180.2	48.0	235.9	7.9				
nt2-7-6.1	Grt core	46	20	0.44	715	10818	1.9	2.1E-3	19	3.90	0.20	7.1	20.3	1.5	0.141	4.4	0.732	7.9	0.0472	1.7	0.210	297.6	4.8	275.6	4.7				
nt2-7-7.1	Amp-Qz-Ttn	280	112	0.42	447	18722	10.5	3.5E-3	14	6.38	0.05	1.2	21.4	1.5	0.103	6.2	0.315	20.1	0.0438	1.8	0.087	276.3	4.8	276.1	4.6				

Notes: analysis name follows the convention w-x-y-z, where w = sample number, x = slide number, y = grain number and z = spot number. SHRIMP analysis employed the instrumental conditions described in Stern (1997). Uncertainties reported at 1 $\sigma$ , calculated using SQUID 2.22.08.04.30. f(206)/207 refers to the mole percent of total <sup>206</sup>Pb that is due to common Pb, calculated using the <sup>207</sup>Pb-method; Stacey and Kramers (1975) model common Pb composition (t = 270 Ma) was used. \* refers to radiogenic Pb (corrected for common Pb). Calibration standard Temora2; <sup>206</sup>Pb/<sup>238</sup>U age = 416.8 Ma (Black et al., 2004). Analyses of a secondary zircon standard (6266) were interspersed between the sample analyses to verify the accuracy of the U–Pb calibration. The accepted <sup>206</sup>Pb/<sup>238</sup>U age of 6266 is 559 Ma  $\pm$  0.2 Ma, based on 22 isotope dilution fractions (Stern and Amelin, 2003). Analytical details: mount IP714, error in <sup>206</sup>Pb/<sup>238</sup>U calibration was 1.02 % (included), standard error in calibration was 0.40 % (not included in above errors but required when comparing data from different mounts), 12  $\mu$ m diameter spot, 2 nA O<sub>2</sub> – primary beam, 6 scans. Using the calibration defined by the Temora2 standard, the weighted mean <sup>206</sup>Pb/<sup>238</sup>U age (207Pb-method) of 16 SHRIMP analyses of 6266 zircon was 556.4  $\pm$  3.4 Ma (95% confidence).

Table 4: Compilation of  $P$ - $T$ -time data for the Sumdo complex, in chronological order. \*MSWD not available for some data. For Ar-Ar data, % of plateau that is  $^{39}\text{Ar}$  is quoted as a guide to data quality. Age data with MSWD  $> 5$  or  $2\sigma$  errors  $> 10\%$  are not reported. Where not specified, errors of  $\pm 1$  kbar and  $50^\circ\text{C}$  are applied as a minimum estimate of uncertainty ( $2\sigma$ ; Powell and Holland, 2008; Palin et al., 2016). Wr = whole-rock.

Age (Ma)	MSWD/% plateau*	Technique	Unit	Study interpretation	Reference	$P$ (kbar)	$T$ ( $^\circ\text{C}$ )	Location
304 $\pm$ 5	5.0	U-Pb zircon (high Th/U cores)	Eclogite	Protolith age	Cheng et al. (2015)	-	-	Bailang
290.6 $\pm$ 6.2	1.1	U-Pb zircon (high Th/U cores)	Eclogite	Protolith age	Cheng et al. (2012)	-	-	Jilang
273.6 $\pm$ 2.8	1.5	U-Pb zircon	Eclogite	Prograde metamorphism	This study	15.5-16.5	500-560	Sumdo
265.9 $\pm$ 1.1	1.8	Lu-Hf Wr-Grt-Omp	Eclogite	Eclogite-facies metamorphism	Cheng et al. (2012)	34-38	750-790	Jilang
262 $\pm$ 5	1.1	U-Pb zircon	Eclogite	Eclogite-facies metamorphism	Yang et al. (2009)	27 $\pm$ 1	730 $\pm$ 50	Sumdo
241 $\pm$ 3	90%	Ar-Ar Ms	Schist	Cooling age	Li et al. (2012)	-	400 $\pm$ 50	Bailang
239.0 $\pm$ 3.5	-	Sm-Nd Wr-Grt-Omp	Eclogite	Eclogite-facies metamorphism	Zeng et al. (2009)	26 $\pm$ 1	650 $\pm$ 50	?
234 $\pm$ 3	89%	Ar-Ar Ms	Eclogite	Cooling age	Li et al. (2012)	-	400 $\pm$ 50	Sumdo
230.0 $\pm$ 4.7	0.3	Sm-Nd Wr-Grt-Omp	Eclogite	Eclogite-facies metamorphism	Cheng et al. (2015)	26 $\pm$ 1	465-505	Bailang
230 $\pm$ 2	94%	Ar-Ar Ms	Schist	Cooling age	Li et al. (2012)	-	400 $\pm$ 50	Bailang
230 $\pm$ 2	82%	Ar-Ar Ms	Eclogite	Cooling age	Li et al. (2012)	-	400 $\pm$ 50	Jilang
224 $\pm$ 2	94%	Ar-Ar Ms	Eclogite	Cooling age	Li et al. (2012)	-	400 $\pm$ 50	Bailang

**Fig. S1.** Sample nt2  $T$ - $M_{\text{H}_2\text{O}}$  phase equilibria diagram at 25 kbar. The  $\text{H}_2\text{O}$  phase boundary is highlighted in dark blue. Peak assemblage is shown in red text. The same model conditions are used as in Fig. 6, with the bulk composition varying from anhydrous to renormalised with 5 mol.%  $\text{H}_2\text{O}$ . The diagram shows that only 1 mol.%  $\text{H}_2\text{O}$  is required to saturate the peak assemblage. Therefore, even if  $\text{H}_2\text{O}$ -undersaturated conditions may have prevailed at some point on the prograde  $P$ - $T$  path, e.g. due to the growth of hydrous phases such as lawsonite (Clarke et al., 2006), at some point  $\text{H}_2\text{O}$ -saturated conditions are likely to have been re-encountered, such that reactions associated with forming the peak assemblage could proceed.

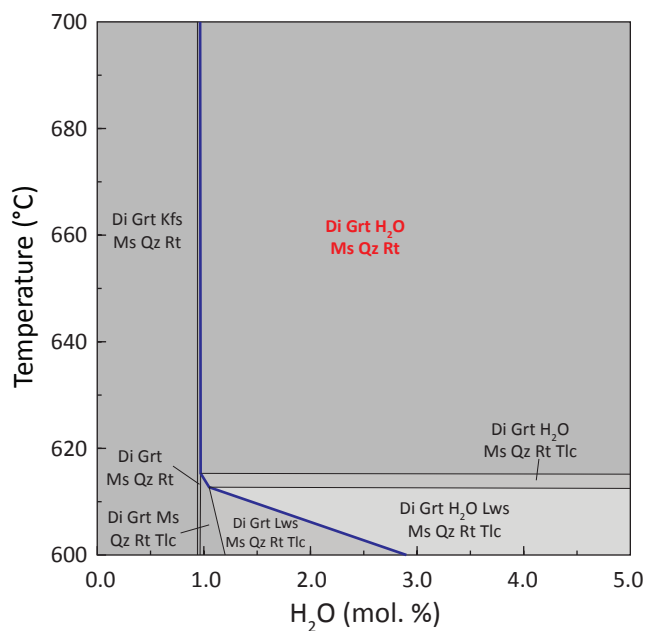


**Table S1.** Ilmenite, Rutile and Titanite WDS data. T = temperature, calculated following Watson et al. (2006).

Analysis	Location	Oxide (wt.%)											Zr (ppm)	T (°C)
		TiO <sub>2</sub>	ZrO <sub>2</sub>	SiO <sub>2</sub>	Cr <sub>2</sub> O <sub>3</sub>	Al <sub>2</sub> O <sub>3</sub>	Nb <sub>2</sub> O <sub>5</sub>	FeO	MnO	MgO	CaO	Total		
ilmenite 1-4 1	matrix	52.06	0.0000	0.00	0.01	0.01	0.00	43.75	2.72	0.15	0.03	98.72	0	-
ilmenite 1-4 2	matrix	51.38	0.0002	0.02	0.00	0.01	0.02	44.78	2.65	0.16	0.00	99.03	1	-
ilmenite 1-4 3	matrix	52.24	0.0000	0.03	0.00	0.00	0.00	44.72	2.40	0.18	0.01	99.58	0	-
ilmenite 4-2 1	matrix	52.48	0.0000	0.00	0.00	0.01	0.04	43.53	2.85	0.15	0.14	99.19	0	-
ilmenite 4-3 1	matrix	51.75	0.0000	0.02	0.01	0.02	0.00	43.55	2.67	0.14	0.47	98.63	0	-
ilmenite 5-2 1	matrix	51.66	0.0031	0.02	0.00	0.00	0.00	45.69	1.80	0.24	0.14	99.55	23	-
rutile 1-2 1	garnet rim	98.94	0.0337	0.00	0.00	0.01	0.00	0.57	0.03	0.01	0.03	99.63	249	628
rutile 1-2 2	garnet rim	98.91	0.0559	0.00	0.02	0.01	0.00	0.57	0.00	0.00	0.01	99.57	414	669
rutile 3-1 1	garnet rim	98.53	0.0466	0.02	0.00	0.02	0.02	0.66	0.00	0.00	0.07	99.38	345	654
rutile 3-1 2	garnet rim	98.96	0.0354	0.02	0.03	0.02	0.00	0.52	0.00	0.01	0.05	99.64	262	632
rutile 1-4 1	matrix	99.79	0.0039	0.01	0.01	0.00	0.02	0.46	0.00	0.00	0.03	100.33	29	485
rutile 2-1 1	matrix	99.39	0.0101	0.02	0.00	0.01	0.01	0.51	0.00	0.00	0.06	100.01	75	542
rutile 2-1 2	matrix	98.90	0.0396	0.00	0.00	0.02	0.00	0.49	0.02	0.00	0.09	99.55	293	641
rutile 4-2 1	matrix	99.24	0.0092	0.02	0.01	0.02	0.01	0.53	0.00	0.00	0.13	99.95	68	536
rutile 4-3 1	matrix	99.04	0.0050	0.00	0.05	0.00	0.00	0.51	0.00	0.00	0.23	99.85	37	499
rutile 5-2 1	matrix	99.35	0.0067	0.03	0.00	0.02	0.04	0.53	0.02	0.00	0.13	100.13	50	516
rutile 6-1 1	matrix	98.75	0.0055	0.01	0.01	0.11	0.00	0.48	0.01	0.00	0.03	99.40	40	504
titanite 1-3 1	garnet core	38.63	0.0146	30.40	0.01	1.07	0.00	0.65	0.01	0.00	29.23	100.02	108	-
titanite 1-3 2	garnet core	38.78	0.0106	30.27	0.02	1.04	0.03	0.60	0.02	0.00	28.88	99.66	79	-
titanite 1-3 3	garnet core	38.41	0.0076	30.44	0.00	1.15	0.00	0.61	0.01	0.00	28.85	99.47	56	-
titanite 1-3 4	garnet core	38.55	0.0108	30.45	0.00	1.08	0.00	0.88	0.01	0.00	28.77	99.74	80	-
titanite 1-3 5	garnet core	38.50	0.0077	30.41	0.00	0.93	0.03	1.10	0.06	0.00	28.86	99.90	57	-
titanite 1-3 6	garnet core	38.41	0.0089	30.31	0.01	0.93	0.03	1.17	0.02	0.01	28.90	99.80	66	-
titanite 1-3 7	garnet core	39.09	0.0069	30.40	0.00	0.89	0.01	0.92	0.05	0.00	29.16	100.52	51	-
titanite 1-3 8	garnet core	38.68	0.0021	30.50	0.01	1.03	0.02	0.82	0.00	0.01	29.01	100.09	15	-
titanite 1-3 9	garnet core	39.41	0.0098	30.43	0.02	0.97	0.00	0.77	0.01	0.01	28.99	100.62	72	-
titanite 1-4 1	matrix	39.27	0.0009	30.80	0.02	1.00	0.00	0.44	0.02	0.00	29.42	100.97	6	-
titanite 1-4 2	matrix	38.86	0.0014	30.32	0.00	0.97	0.00	0.46	0.05	0.01	29.05	99.73	10	-
titanite 2-1 1	matrix	39.69	0.0051	30.69	0.01	0.72	0.02	0.27	0.01	0.00	29.24	100.64	38	-
titanite 2-1 2	matrix	39.48	0.0017	30.56	0.01	0.66	0.03	0.38	0.03	0.00	29.27	100.42	13	-
titanite 4-2 1	matrix	38.69	0.0000	30.56	0.01	1.13	0.00	0.39	0.03	0.00	28.95	99.76	0	-
titanite 4-3 1	matrix	38.67	0.0000	30.19	0.00	1.00	0.02	0.57	0.03	0.00	28.80	99.28	0	-
titanite 5-2 1	matrix	38.91	0.0029	30.86	0.00	1.20	0.01	0.40	0.03	0.00	29.09	100.50	22	-